

1 **Modelling framework for asynchronous land-atmosphere coupling using**
2 **NASA GISS ModelE and LPJ-LMfire: Design, Application and Evaluation**
3 **for the 2.5ka period**

4

5 Ram Singh^{1,2}, Alexander Koch⁴, Allegra N LeGrande^{2,1}, Kostas Tsigaridis^{1,2}, Riovie D Ramos⁵,
6 Francis Ludlow⁶, Igor Aleinov^{1,2}, Reto Ruedy^{2,3}, Jed O Kaplan⁷

7

8

9 ¹ Center for Climate Systems Research, Columbia University, New York, USA

10 ² NASA Goddard Institute for Space Studies, New York, NY-10025, USA

11 ³ SciSpace LLC, New York, NY, USA

12 ⁴ Department of Earth Sciences, The University of Hong Kong, Hong Kong SAR, China

13 ⁵ Earth Observatory of Singapore, Singapore

14 ⁶ Department of History, School of Histories and Humanities, Trinity College, Dublin 2, Ireland

15 ⁷ Department of Earth, Energy, and Environment, University of Calgary, Calgary AB, Canada

16

17

18 *Correspondence to:* Ram Singh (ram.bhari85@gmail.com)

19

20 **Abstract**

21 While paleoclimate simulations have been a priority for Earth system modelers over the past
22 three decades, little attention has been paid to the period between the mid-Holocene (6ka) and
23 the Last Millennium, although this is an important period for the emergence of complex
24 societies. Here, we consider the climate of 2500 BP (before present or 550 BCE), a period when
25 compared to late preindustrial time, greenhouse gas concentrations were slightly lower, and
26 orbital forcing led to a stronger seasonal cycle in high latitude insolation. To capture the
27 influence of land cover on climate, we asynchronously coupled the NASA GISS ModelE Earth
28 system model with the LPJ-LMfire dynamic global vegetation model. We simulated global
29 climate and assessed our results in the context of independent paleoclimate reconstructions. We
30 also explored a set of combinations of model performance parameters (bias and variability) and
31 demonstrated their importance for the asynchronous coupling framework. The asynchronously
32 coupled model system shows strong vegetation-albedo feedback on climate and is comparatively
33 more sensitive to the bias correction than the internal model variability and green Sahara
34 conditions. In the absence of a bias correction, while driving LPJ-LMfire in the coupling process,
35 ModelE drifts towards colder conditions in the high latitudes of the Northern Hemisphere in
36 response to land cover simulated by LPJ-LMfire. A regional precipitation response is also
37 prominent in the various combinations of the coupled model system, with a substantial
38 intensification of the Summer Indian Monsoon and a drying pattern over Europe. Evaluation of
39 the simulated climate against reconstructions of temperature from multiple proxies and the
40 isotopic composition of precipitation ($\delta^{18}\text{O}_p$) from speleothems demonstrated the skill of ModelE
41 in simulating past climate. A regional analysis of the simulated vegetation-climate response
42 further confirmed the validity of this approach. The NASA GISS ModelE found to be
43 particularly sensitive to the representation of shrubs and this land cover type requires particular
44 attention as a potentially important driver of climate in regions where shrubs are abundant. Our
45 results further demonstrate the importance of bias correction in coupled paleoclimate
46 simulations. This study presents a generalized framework for incorporating biogeophysical
47 responses into climate models without dynamic vegetation, for simulating past climates, in line
48 with the recommendations of the Paleoclimate Modelling Intercomparison Project (PMIP).

49 **1. Introduction**

50 Earth system models (ESMs) are widely applied in paleoclimate experiments as an “out of
51 sample” exercise to evaluate the overall quality of the model, and to better understand climate
52 system responses to external forcings. In many paleoclimate modeling studies, it has been
53 demonstrated that inclusion of biogeophysical and biogeochemical feedbacks between land and
54 atmosphere feedbacks are essential to simulate the magnitude and spatial pattern of climate
55 change that is consistent with independent reconstructions (Betts, 2000; Claussen, 1997; Cox et
56 al., 2000; Doherty et al., 2000; Strandberg et al., 2014a). The importance of land-atmosphere
57 feedbacks for past climate has shown particularly to be true in the context of the mid-Holocene
58 and last glacial inception periods (Braconnot et al., 2012; Collins et al., 2017; Harrison et al.,
59 2015; Jahn et al., 2005; Kubatzki and Claussen, 1998; Sha et al., 2019; Shanahan et al., 2015;
60 Tierney et al., 2017). For example, for the African Humid Period of the mid-Holocene, numerous
61 studies demonstrated that greenhouse gases (CO_2 , N_2O , CH_4) and orbital forcing are alone not
62 sufficient for models to simulate climate that is consistent with independent paleoclimate
63 reconstructions. The inclusion of land-atmosphere feedbacks via interactive dynamic vegetation
64 modeling or prescribed vegetation distributions helps improves model-proxy discrepancies
65 (Chandan and Peltier, 2020; Charney, 1975; Dallmeyer et al., 2021; Pausata et al., 2016;
66 Rachmayani et al., 2015; Singh et al., 2023; Thompson et al., 2021; Tiwari et al., 2023;
67 Velasquez et al., 2021). For this reason, more recent protocols (PMIP4; Otto-Bliesner et al.,
68 2017) for simulations of the mid-Holocene specify that the land cover boundary condition should
69 include shrub vegetation in northern Africa with greater extent than the present (the so-called
70 “Green Sahara”), as well as an expansion of trees and shrubs at high northern latitudes.

71
72 Instead of prescribing land cover boundary conditions in an earth system model, it may be
73 desirable to employ a coupled model where that allows interaction between climate and
74 vegetation. While several modern earth system models include a dynamic representation of land
75 cover, in climate models (regional and global) that lack a coupled dynamic vegetation
76 component a well-established technique to capture land-atmosphere feedbacks is to use
77 asynchronous coupling. In this type of coupling, climate model output is used to drive an offline
78 vegetation model that then returns a land cover boundary condition to the climate model.

79 To quantify the feedback between land and atmosphere and improve the fidelity of the
80 paleoclimate simulation, asynchronous coupling typically involves running a climate model
81 simulation for a period of a few decades, after which the mean climate state is passed to a
82 vegetation model that in-turn produces a land cover boundary condition for the climate model.
83 This process is repeated until climate reaches equilibrium, defined as insignificant changes in
84 key outputs, e.g., 2m temperature, from one cycle to the next.

85
86 (Texier et al., 1997) used the iterative asynchronous coupling between the LMD Atmospheric
87 General Circulation Model (AGCM) and the BIOME1 vegetation model to produce an improved
88 climate for the mid-Holocene (6ka) period and found that inclusion of land-atmosphere
89 feedbacks led to simulations of temperatures at high latitudes and precipitation over West Africa
90 that were more consistent with independent paleoclimate reconstructions compared to
91 atmosphere-only simulations. (de Noblet et al., 1996) used a similar coupling to highlight the
92 role of biogeophysical feedback in glacial initiation around 115ka ago. Asynchronous coupling
93 has also been used with regional climate models (RCMs). (Kjellstroem et al., 2009) and
94 Velasquez et al. (2021) both used asynchronous coupling between an RCM and land cover
95 model to simulate the climate of Europe at the Last Glacial Maximum. Both studies
96 demonstrated the importance of land cover in improving the agreement with reconstructions and
97 paleoenvironmental proxies.

98
99 This study has two objectives. First, we present a generalized design for asynchronously
100 coupling the NASA GISS ModelE2.1 climate model (Kelley et al., 2020) with the LPJ-LMfire
101 DGVM (Pfeiffer et al., 2013) to simulate climate including biogeophysical land-atmosphere
102 feedbacks. Second, we demonstrate the utility of this asynchronous coupling framework for a
103 paleoclimate period that has not been the traditional focus of paleoclimate modeling (2.5ka) and
104 evaluate the model results against independent paleoclimate reconstructions for that period.

105
106 2.5ka represents a time that is nearest to the present day among the different periods selected
107 under the coordinated effort of the Paleoclimate Model Intercomparison Project (PMIP4). It is
108 interesting because it represents an important period for the emergence of complex societies
109 across Eurasia (Iron Age, Classical Antiquity, early Imperial China) and elsewhere. During this

110 era, favorable climate conditions around the Mediterranean might have influenced the emergence
111 of the golden age of Greece, the Roman classical period, and other empires of the Southern
112 Europe, North Africa, and southwest Asia (Lamb, 1982; Reale and Dirmeyer, 2000). On the
113 other hand, adverse climate conditions due to volcanic eruptions and a series of arid phases
114 during this period may have had a negative impact on Egyptian civilization around the Nile and
115 Mesopotamian civilization around the Euphrates and Tigris rivers. 2.5ka is thus a key period for
116 the study of human-environment interactions and the history of climate and society, where we
117 may assess societal vulnerability to climate change (Ludlow and Manning, 2021; Manning et al.,
118 2017; Mikhail, 2015; Petit-Maire and Guo, 1998; Singh et al., 2023).

119 Section 2 describes the models used in this study (Section 2.1), the initial control run for 2.5ka,
120 and a stepwise description of the asynchronous coupling framework, including variable exchange
121 and processing (Sections 2.2 and 2.3). Section 3 presents the experimental design for
122 implementing the asynchronous coupled system and evaluates the PFT mapping schemes. In
123 Section 4, we evaluate the simulated 2.5ka climate using the ModelE–LPJ asynchronous
124 coupling framework against multi-proxy temperature reconstructions (Kaufman et al., 2020) and
125 additionally utilized the model’s capabilities to simulate the isotopic composition of water in
126 precipitation ($\delta^{18}\text{O}_p$) to compare with the Speleothem Isotope Synthesis and Analysis (SISAL)
127 version 2 database (Comas-Bru et al., 2020). Section 5 provides the analysis and comparison of
128 model-simulated climate under various experimental configurations.

129

130 **2. Models and asynchronous coupling framework**

131 **2.1.1 NASA GISS ModelE2.1:** NASA GISS ModelE2.1 (Kelley et al., 2020), is the climate model
132 of the NASA Goddard Institute for Space Studies (GISS) currently used in Climate Model
133 Intercomparison Project (CMIP) phase 6 (Eyring et al., 2016). We used the NINT (Non-
134 Interactive; physics version 1 in CMIP6) GISS ModelE2.1 version where aerosols and ozone are
135 precomputed from the prognostic, but much more computationally demanding, chemistry and
136 aerosols version of the model OMA (One Moment Aerosols; physics version 3 in CMIP6; (Bauer
137 et al., 2020)). In our simulations, the GISS ModelE2.1 atmosphere has a horizontal resolution of
138 $2^\circ \times 2.5^\circ$ (latitude/longitude) with 40 vertical layers, and the top of the atmosphere at 0.1 hPa. The
139 ModelE2.1 atmosphere has a smooth transition from sigma layers to constant pressure layers
140 centered at 100hPa. The atmosphere is coupled to the GISS Ocean v1 model, which runs at a

141 resolution of $1^{\circ} \times 1.25^{\circ}$ (latitude/longitude) with 40 depth layers to the ocean bottom. While the
142 biogeophysical properties of land cover are simulated with the Ent Terrestrial Biosphere Model
143 (Ent TBM; Kiang 2012; (Kim et al., 2015)), as part of ModelE2.1 (Ito et al., 2020), Ent relies on
144 a prescribed vegetation map and as such does not simulate changes in land cover over time. To
145 capture the influence of climate change on land cover and biogeophysical feedbacks between land
146 and atmosphere, asynchronous coupling with LPJ-LMfire (or any other DGVM) is currently
147 required.

148
149 **2.1.2 LPJ-LMfire:** We used the LPJ-LMfire DGVM (v1.4.0) to simulate the land cover
150 boundary conditions in our experiments. LPJ-LMfire (Kaplan et al., 2022; Pfeiffer et al., 2013) is
151 an evolution of LPJ (Sitch et al., 2003) and is a process-based, large-scale representation of plant
152 growth and decay, vegetation demographics and ecological disturbance, and water and carbon
153 exchanges between the land and the atmosphere. LPJ-LMfire has been successfully validated for
154 simulating present-day biogeography and fire regime characteristics, and its outputs have been
155 compared against contemporary observations (Pfeiffer et al., 2013; Sitch et al., 2003; Thonicke
156 et al., 2010). For this study, we simulated land cover boundary conditions at a horizontal
157 resolution $0.5^{\circ} \times 0.5^{\circ}$. LPJ-LMfire is driven by monthly fields of climate (temperature,
158 precipitation, cloud cover, wind, and lightning), static maps of topography and soil texture, and
159 an annual global value of atmospheric CO_2 concentration. LPJ-LMfire simulates land cover in
160 the form of fractional coverages of nine plant functional types (PFTs), including tropical,
161 temperate, and boreal trees, and tropical and extratropical herbaceous vegetation (Table 1). CO_2 ,
162 soil texture and topography data used to drive LPJ-LMfire are described in Pfeiffer et al. (2013,
163 Table 3). For 2.5ka simulations, we set atmospheric CO_2 concentrations to 271.4 ppm (Kaplan et
164 al., 2012). The sum of PFT fractional cover per grid box does not need to equal unity; when it is
165 less than one the remainder is considered bare ground.

166
167 **Table 1:** - Summary of climate and PFT variables exchanged between NASA GISS ModelE and
168 LPJ-LMfire model for asynchronous coupling process. Column 1 and 2 shows list the output and
169 input climate variables from GISS ModelE to LPJ-LMfire models, whereas the columns 3 and 4
170 lists the output and input plant function types (PFTs) from LPJ-LMfire to GISS ModelE.

| GISS Output | LPJ -LMfire Input | Annual cycle climatology and variability (standard deviation) over the period of interest (100 Years) | LPJ-Lmfire Output Vegetation (PFTs) | LPJ-LMfire to GISS ModelE (Ent) Vegetation Mapping (Vegetation cover type, Leaf area index and vegetation heights) | GISS ModelE (Ent) Vegetation (PFTs) |
|---|--|--|--|---|--|
| Surface Air Temperature (°C) | Surface Air Temperature (°C) | | Tropical Broadleaf Evergreen | | Evergreen Broadleaf Late Succession |
| Precipitation (mm/day) | Precipitation (mm/day) | | Tropical Broadleaf Raingreen | | Evergreen Needleleaf Late Succession |
| | Number of wet days | | | | |
| Diurnal Surf. Air Temp Range (°C) | Diurnal Surf. Air Temp Range (°C) | | Temperate Needleleaf Evergreen | | Cold Deciduous Broadleaf Late Succession |
| Surface Wind Speed (m/sec) | Surface Wind Speed (m/sec) | | Temperate Broadleaf Evergreen | | Drought Deciduous Broadleaf |
| Moist Convective Air Mass Flux (kg/m ² /sec) | Lightning Density (strokes/Km ² /day) | | Temperate Broadleaf Summergreen | | Deciduous Needleleaf |
| | | | Boreal Needleleaf Evergreen | | Cold Adapted Shrub |
| | | | Boreal Summergreen | | Arid Adapted Shrub |
| | | | C3 Perennial Grass | | C3 Grass Perennial |
| | | | C4 Perennial Grass | | C4 Grass |
| | | | | | C3 Grass Annual |
| | | | | | Arctic C3 Grass |
| | | | Bright Bare Soil | | |
| | Dark Bare Soil | | | | |

173

174 **2.2. 2.5ka Simulation setup (Initial control run using ModelE)**

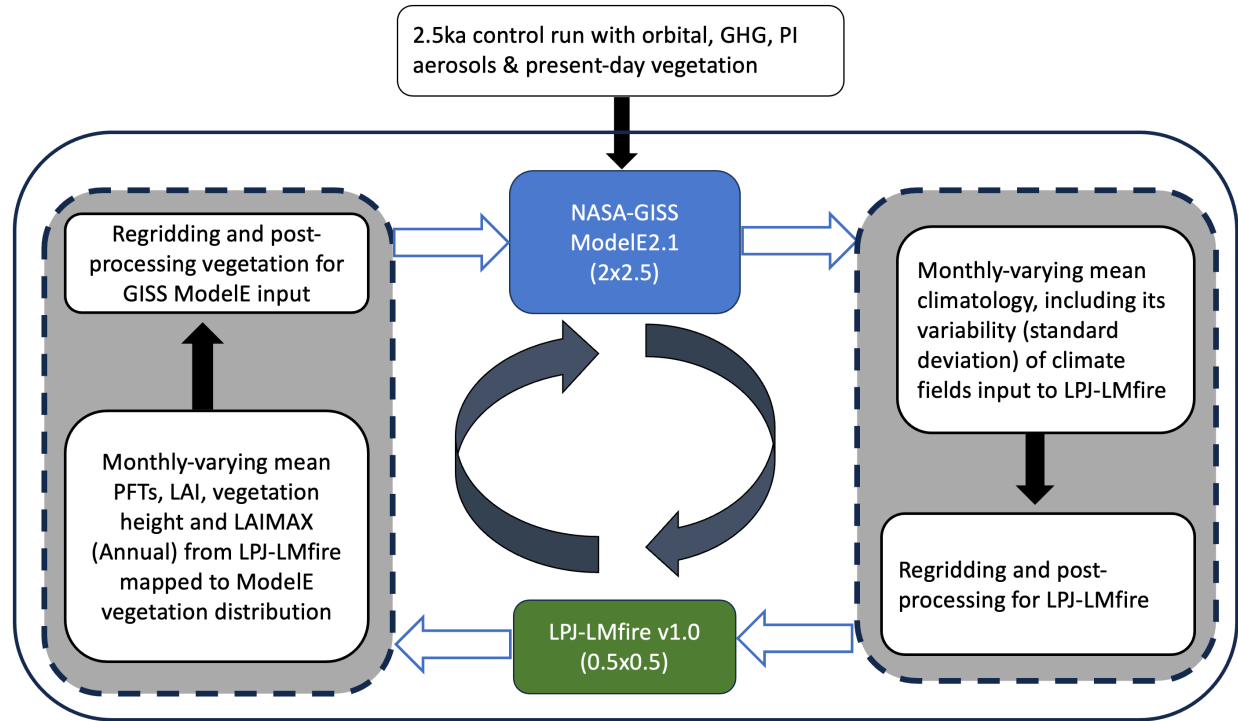
175 We started the 2.5ka and preindustrial (PI) control experiments following the PMIP4 and CMIP6
176 protocols (Eyring et al., 2016; Kageyama et al., 2018). The PI simulation uses preindustrial (year
177 1850) GHG concentrations and a modern continental configuration and serves as the reference
178 experiment for designing the boundary conditions for past time slices studied in PMIP4. GHG and
179 orbital forcings for the preindustrial (PI) control experiment correspond to levels observed in
180 1850 CE (CO₂: 284 ppm, N₂O: 273 ppb, CH₄: 808 ppb). For the 2.5ka control experiment, orbital
181 parameters (Berger et al., 2006) were specified for 2,500 years BP (before present ~550 BCE), and
182 greenhouse gas CO₂, N₂O, and CH₄ were set to ~279 ppm, ~266 ppb, and 610 ppb respectively
183 (Köhler et al., 2017; Loulergue et al., 2008; Otto-Bliesner et al., 2017; Schneider et al., 2013;
184 Siegenthaler et al., 2005). We considered only natural emissions as sources of aerosols in the
185 atmosphere, zeroing-out any anthropogenic contribution to aerosol and aerosol precursors. For
186 biomass burning, in the absence of any better estimate, we assumed that the emissions provided
187 by CEDS (Hoesly et al., 2018) for the year 1750 are all natural. Land cover consists of the
188 fractional coverages of 13 plant functional types (PFTs) and includes vegetation height and leaf
189 area index (LAI). For the PI and initial (0th order) simulations, land cover type and monthly-
190 varying LAI were derived from satellite (MODIS) data (Gao et al., 2008; Kattge et al., 2011;
191 Myneni et al., 2002; Tian et al., 2002a, b; Yang et al., 2006) and vegetation heights from (Simard
192 et al., 2011). We also used the mid-Holocene (6k) vegetation under PMIP4 protocol, which is
193 linearly interpolated to 2.5ka period and details of vegetation cover changes (Singh et al., 2023;
194 Figure S1) and associated impacts on the northern hemisphere climate due to the inclusion of
195 scaled PMIP4 vegetation using the interactive chemistry version of NASA GISS ModelE2.1
196 (MATRIX) are discussed in (Singh et al., 2023).

197

198 **2.3 Asynchronous coupling framework**

199 The asynchronous coupling between ModelE and LPJ-LMfire is summarized in Figure 1. For each
200 iteration, ModelE simulated climate is used by LPJ-LMfire, which, returns the PFT fractional
201 cover, LAI, and vegetation height that are used as boundary conditions for the next ModelE
202 simulation.

203



204

205 Figure 1: Flow diagram for the asynchronous coupling framework between GISS ModelE2.1 and
 206 LPJ-LMfire models. For the climate fields input to LPJ-LMfire refer to (Table 1, Column 1) and
 207 LPJ-LMfire PFTs (Table 1, Column 3)

208

209 **2.3.1 GISS ModelE2.1 simulations:** Climatological monthly mean climate (Table 1, Column 1)
 210 for a 100-year period were extracted from a well equilibrated ModelE simulation. To assess
 211 interannual variability with monthly resolution, we calculated the standard deviation of the decadal
 212 mean data for each month across the 100-year equilibrium period.

213 **2.3.2. LPJ-LMfire simulations:** All climate variables except diurnal temperature range, wet days,
 214 and lightning density were provided directly from the ModelE output. For derived climate
 215 variables, the additional processing steps are described below.

216

217 Diurnal temperature range was calculated as the difference of the monthly-mean daily maximum
 218 and minimum temperatures as simulated by ModelE. Wet days were calculated from modelled
 219 precipitation based on an empirical relationship between present-day monthly total precipitation
 220 and the number of wet days per month. To quantify this relationship, we performed a nonlinear
 221 regression between monthly total precipitation and number of days with measurable precipitation
 222 using the CRU TS 4.0 gridded climate fields (Harris et al., 2020). Using those data, we developed

223 a set of regression coefficients for every land gridcell that allowed us to estimate wet days for any
224 paleoclimate period based only on monthly total precipitation. Lightning density was estimated
225 based on modelled convective mass flux following Magi (2015). However, the feedback to climate
226 due to fire-driven emissions are not included, as accounting for them would require active
227 atmospheric chemistry and transport, which are not included in LPJ-LMfire.

228

229 Because LPJ-LMfire requires a timeseries of interannually varying climate forcing to run, we
230 processed the climatological monthly mean climate produced by the ModelE for use with the
231 vegetation model. In brief, ModelE climate was converted into anomalies by differencing the
232 paleoclimate simulation with ModelE simulated climate for the late 20th century (1951-2000). The
233 resulting climate anomalies were bilinearly interpolated to a 0.5°x0.5° grid and added to a baseline
234 climate based on observations over 1951-2000. The resulting climatology was expanded to a 1020-
235 year-long time series by adding interannual variability in the form of detrended and randomized
236 climate anomalies from the 20th Century Reanalysis (Compo et al., 2011). LPJ requires climate
237 input data with interannual variability because fires and other disturbance events occur only in
238 years with anomalous climate, for example, hot or dry years Sitch et al. (2003). Driving the model
239 with climatological mean climate will result in disturbance frequencies that are lower than the
240 expected mean that in some regions would lead to an overabundance of tree cover when we would
241 expect herbaceous vegetation. For further details on this process, see (Hamilton et al., 2018).
242 Because LPJ-LMfire is computationally inexpensive, we ran each simulation for 1020 years.
243 While the composition and characteristics of aboveground vegetation comes into equilibrium with
244 climate after a few centuries of simulation, a millennium-long simulation brings the terrestrial
245 carbon pools into equilibrium as well. The land cover boundary conditions returned to the climate
246 model represent the mean modeled vegetation cover over the final 250 years of the LPJ-LMfire
247 simulation.

248

249 **2.3.3. LPJ-LMfire to GISS ModelE vegetation mapping:** LPJ-LMfire simulates land cover in
250 the form of nine PFTs, while in GISS ModelE the vegetation component (Ent TBM) recognizes
251 13 PFTs. We mapped the LPJ-LMfire generated PFT cover, LAI, LAIMAX, and vegetation height
252 to the GISS ModelE2.1 (Ent) PFTs in order to feed it to the ModelE (Table 1, Column 3 & 4). The
253 main points for the LPJ-LMfire to GISS vegetation mapping are the following:

254
255
256
257
258
259
260
261
262
263
264
265
266
267
268
269
270
271
272
273
274
275
276

- Early and late-successional PFTs were approximated from the LPJ-LMfire output using the model simulated fire frequency and monthly burned area fraction. High fire frequency favors early-successional PFTs because the time between disturbances is shorter than that required for establishment. By definition, late-successional PFTs require extended periods of low disturbance to persist within the ecosystem. However, because successional state is indistinguishable in the satellite-driven reference vegetation for the historical period used as the boundary condition for ModelE, we combined early & late successional PFTs in our simulations.
- LPJ-LMfire does not have a specific PFT for shrubs (arid and cold), while Ent does. To estimate shrub cover in LPJ-LMfire, we used LPJ-LMfire simulated tree height for the tropical broadleaf raingreen, temperate broadleaf summergreen, and boreal summergreen PFTs and specified that trees with height lower than a globally-uniform predefined threshold were considered to be shrubs (Table S1).
- Ent has an Arctic grass PFT while LPJ-LMfire does not. To estimate Arctic grass cover we used the C₃ grass PFT in LPJ-LMfire and specified it as Arctic grass in regions where the boreal summergreen PFT was also present. LPJ-LMfire also does not distinguish between annual and perennial grasses, and so to map these to Ent we assumed that these were present in equal fractions among the simulated C₃ grass in the LPJ-LMfire simulation.
- The non-vegetated fraction of a grid cell is assigned to the bare soil, and the distribution of bright and dark soil color heterogeneity is classified/redistributed based on the present-day structure of soils over a grid cell.

277 Of particular importance to our coupled model simulations was that the PFTs simulated by LPJ-
278 LMfire do not explicitly include a shrub type. To approximately distinguish tree from shrub cover,
279 we generated three LPJ-to-GISS mapping schemes that differed on how shrubs are specified. A
280 set of possible changes in various PFT classifications are adopted based on the comparison with
281 GISS vegetation distribution and categorized the mapping methodologies. These mappings,
282 summarized in table S1, differ in the height threshold of trees to be re-categorized as cold and arid
283 shrubs, and the fraction of perennial grass re-categorized into perennial and arctic grasses. Also,

284 the monthly leaf area index (LAI) and vegetation height readjusted using the weighted mean for
285 remapped LPJ-LMfire vegetation PFTs.

286

287 **2.3.4. Step 4. Post-processing of vegetation files:** LPJ-LMfire model generates output at a
288 horizontal resolution of $0.5^{\circ} \times 0.5^{\circ}$. We resampled the output vegetation information to the
289 $2.0^{\circ} \times 2.5^{\circ}$ grid used by ModelE2.1. In a few cases, land cover extrapolated using a nearest-neighbor
290 approach was to cover all the gridcells identified as land in the ModelE standard land-sea mask.

291

292 **3 Experimental Design**

293 Apart from evaluating the framework for the PI control period, we designed a set of experiments
294 to evaluate various aspects of the simulated climate, including model bias, and variability in both
295 the climate and vegetation models. For example, one known limitation in the current version of
296 ModelE is a wintertime cold bias over the Arctic in simulations covering the historical period
297 (Kelley et al., 2020).

298

299 Table 2 shows the combinations of the model metrics selected to explore the utility of the
300 asynchronous coupling framework and their impact on simulated climate. Run names are
301 designated using Time (1850, 2.5k), Vegetation source (PI, GS), Bias Correction (BC) and
302 Interannual Variability (LPJ, GISS) separated by “_”. For example, ‘1850_PI_ctrl’ and
303 ‘2.5k_PI_ctrl’ denote the 1000-year-long PI and 2.5k runs with GISS PI vegetation. GS stands for
304 Green Sahara and PI = Pre-Industrial. An “x” denotes the absence of a particular criterion (default
305 state). Run ‘1850_PI_ctrl’ (row 1 in table 2) was performed to evaluate the vegetation mapping
306 scheme and to select the appropriate scheme for asynchronous coupling, whereas ‘2.5k_PI_ctrl’
307 (row 2 in table 2) is used as the 0th order control run for 2.5ka period with present-day vegetation
308 distribution. Runs ‘2.5k_PI_BC_LPJ’, ‘2.5k_PI_x_x’, and ‘2.5k_PI_x_GISS’ are three branches
309 extended from ‘2.5k_PI_ctrl’ with the combinations of bias correction and interannual variability
310 from LPJ and GISS models. For the ‘2.5k_GS_x_GISS’ and ‘2.5k_GS_BC_GISS’ simulations,
311 we initialized the land cover boundary conditions to approximate 2.5ka by linearly interpolating
312 cover fractions between the 6ka land cover prescribed under the PMIP4 protocol (Otto-Bliesner et
313 al., 2017) and the PI reference dataset and extended the 0th order 2.k control (‘2.5k_PI_ctrl’) before
314 branching out the experiments ‘2.5k_GS_x_GISS’ and ‘2.5k_GS_BC_GISS’. Details of the 6ka

315 land cover boundary conditions under for PMIP4 and associated impacts on Northern Hemisphere
316 climate using the interactive chemistry version of NASA GISS ModelE2.1 (MATRIX) are
317 discussed by (Singh et al., 2023). Model equilibrium is determined using the threshold that the
318 absolute value of the decadal-mean planetary radiative imbalance must be $< 0.2 \text{ W m}^{-2}$, along with
319 the surface temperature trend (absolute value $< 0.1 \text{ }^{\circ}\text{C}/50 \text{ years}$). Convergence across iterations is
320 evaluated by comparing the annual mean climate state and vegetation distributions between
321 successive iterations.

322 **Table 2:** - Summary of experiment designs followed to explore and evaluate the GISS ModelE -
 323 LPJ-LMFire model asynchronous coupling framework. See text for an explanation on the run
 324 naming convention.

| Run Name | Initial Vegetation Cover | Bias correction | Interannual Variability | Number of Iterations/total number of years | Remark |
|-----------------|--|-----------------|-------------------------|--|---|
| 1850_PI_ctrl | Used to evaluate the LPJ to GISS vegetation mapping schemes GHG Forcing: CO ₂ : 284 ppm, N ₂ O: 273 ppb, CH ₄ : 808 ppb | | | | |
| 2.5k_PI_ctrl | 1000-year-long control; base run to branch out the other simulations GHG Forcing: CO ₂ : 279 ppm, N ₂ O: 266 ppb, and CH ₄ : 610 ppb | | | | |
| 2.5k_PI_BC_LPJ | GISS PI vegetation | YES | LPJ | 5/750 years | converged |
| 2.5k_PI_x_x | GISS PI vegetation | No | No | 2/270 years | Too cold in 3 rd iteration diverging |
| 2.5k_PI_x_GISS | GISS PI vegetation | No | GISS ModelE (100years) | 4/550 years | Too cold diverging |
| 2.5k_GS_x_GISS | GISS PI vegetation + Green Sahara+ Boreal Forest | No | GISS ModelE (100years) | 5/1150 years | Too cold diverging |
| 2.5k_GS_BC_GISS | GISS PI vegetation + Green Sahara+ Boreal Forest | YES | GISS ModelE (100years) | 4/1000 years | converged |

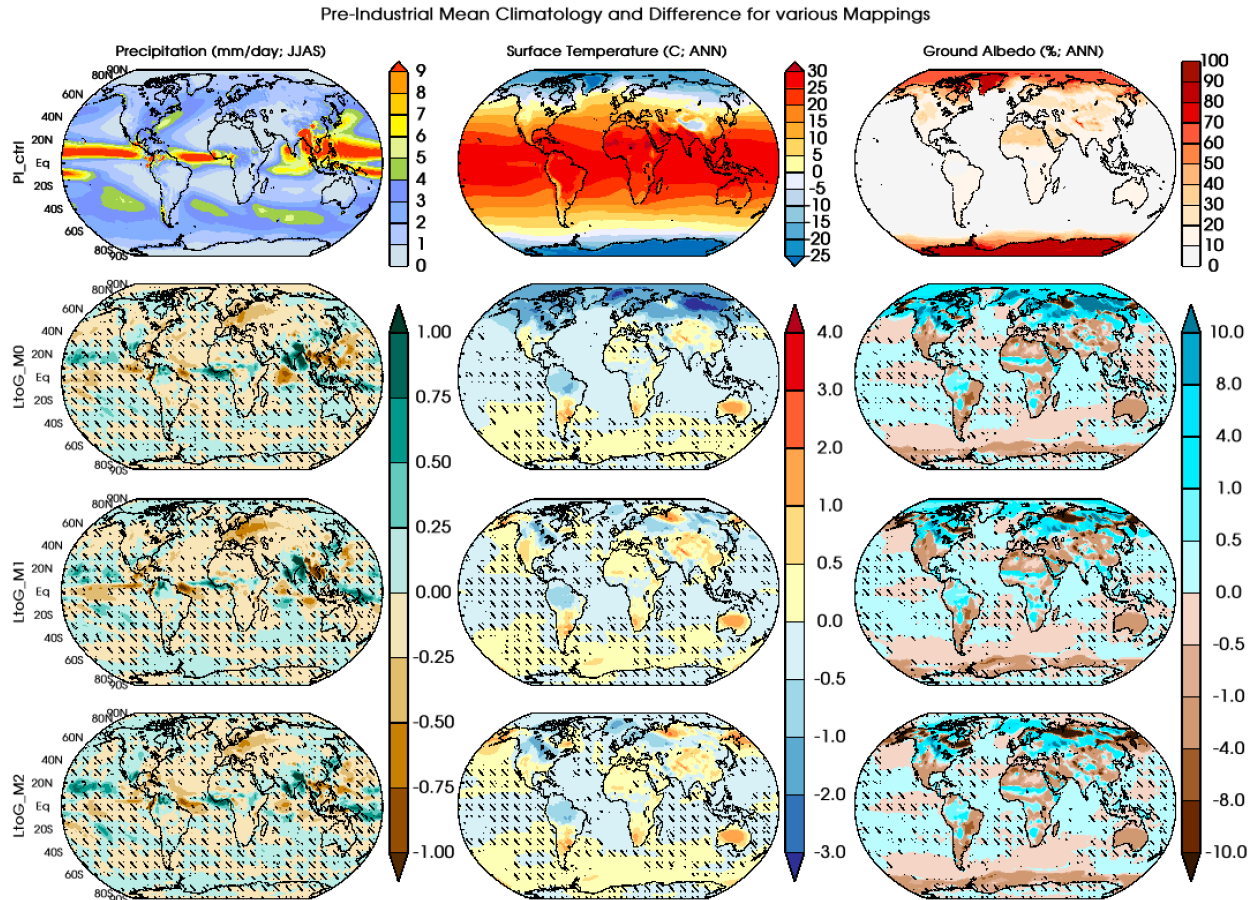
325 * Convergence means the final model simulation has a similar climatology with the previous
 326 iteration, whereas divergence means the model is drifting away from the expected states.

327
 328

329 **3.1 Evaluation & Validation of LPJ-GISS Mapping Methodologies**

330 We used the standard present-day land cover boundary conditions described for ModelE2.1
331 (Kelley et al., 2020) for the initial 0th-order iteration of the pre-industrial and 2.5ka control
332 climate simulations. This land cover dataset is based on satellite observations (Gao et al., 2008;
333 Myneni et al., 2002; Tian et al., 2002a, 2002b; Yang et al., 2006) from the Moderate Resolution
334 Imaging Spectroradiometer (MODIS), with leaf area index (LAI) from the TRY database (Kattge
335 et al. 2011), and vegetation height (Simard et al. 2011) from the Geoscience Laser Altimeter
336 System (GLAS). Branches of the 2.5ka run for green Sahara conditions are started using the
337 linearly interpolated vegetations for 2.5ka from the 6ka vegetation distribution defined based on
338 the PMIP4 protocol (Otto-Bliesner et al., 2017; Singh et al., 2023). These land cover boundary
339 conditions are shown as the fractional coverage of 13 PFTs (including bare soils) (Figs. S1.A and
340 S1.B). In these figures, bare dark and bare bright are merged into a single bare soil fractional
341 cover.

342
343 The ModelE2.1 pre-industrial (PI) control run initialized with the present-day land cover boundary
344 condition is processed through the asynchronous coupling framework to evaluate the mapping
345 scheme for converting LPJ PFTs to GISS (Ent) PFTs. We tested three sets of LPJ-to-GISS
346 mapping schemes as required in the asynchronous coupling framework. Differences among the
347 mapping schemes are described in supplementary table TS1. Three parallel control runs are
348 performed for 100 years, each initialized with the vegetation distribution that corresponds to the
349 corresponding mapping scheme and compared to the mean climate state of the parent PI control
350 run.
351



352
 353 **Figure 2.** Comparison of seasonal mean climate metrics when using different vegetation mapping
 354 schemes with that of the original PI control. Top row shows the mean climatology for precipitation
 355 (mm/day; JJAS), surface air temperature (°C; ANN) and ground albedo (%; ANN) and row 2 to 4
 356 shows the differences in mean climate for the mappings LtoG_M0, LtoG_M1 and LtoG_M2,
 357 respectively. Stippling indicates the region over which change is not statistically significant at a
 358 95% confidence interval (Used the student's t-test).

359
 360 The mapping schemes LtoG_M1 and LtoG_M2 (supplementary table TS1) generate a similar
 361 spatial structure of annual surface air temperature with broadly similar regional characteristics
 362 (Fig. 2). A shift towards colder climates of 2-3 °C in mean annual temperature over the higher
 363 latitudes of the Northern hemisphere is simulated when using the mapping scheme LtoG_M0,
 364 which is not present when using the other mapping schemes (LtoG_M1 and LtoG_M2). We
 365 selected forests into shrubs to match the missing PFTs in ModelE vegetation distributions based
 366 upon the tree height (Table S1). In these mapping schemes, the fraction of boreal tree PFTs

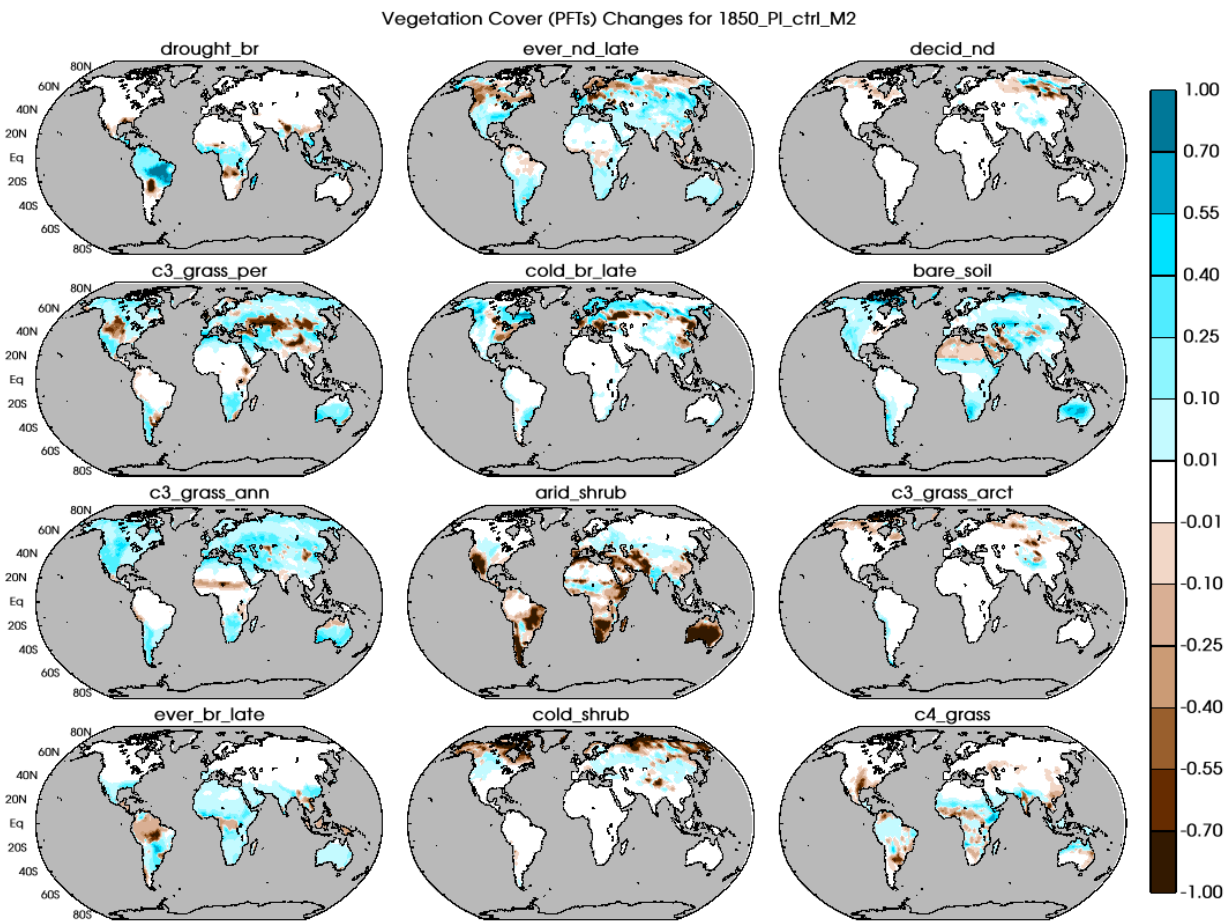
367 assigned to cold shrubs depends on simulated tree height, which is, in turn, influenced by surface
368 temperature (Bonan, 2008; Bonan et al., 1992; Li et al., 2013; Thomas and Rowntree, 1992). In
369 the mapping LtoG_M0, the fractional cover of boreal tree PFTs was reduced significantly,
370 leading to an increase in ground albedo (up to 10%), which led to the model drifting towards
371 comparatively colder climate conditions. When using the other two mapping schemes (LtoG_M1
372 and LtoG_M2) the assignment of boreal tree PFTs to shrub types is limited by a higher tree
373 height threshold and partially because other PFTs (perennial grass) are substituted for cold
374 shrubs. Regional patches of increased ground albedo and surface cooling over the higher
375 latitudes of the Northern Hemisphere are also evident when using the LtoG_M1 and LtoG_M2
376 translation schemes.

377
378 Precipitation during the Northern Hemisphere summer monsoon season (JJAS; June-July-
379 August-September) appears similar among the three mapping schemes, as the larger changes are
380 confined to the equatorial regions. A drying pattern over Europe appears in all three translation
381 schemes, but it is comparatively more substantial under LtoG_M0 and LtoG_M1 than LtoG_M2.

382
383 All translation schemes also lead to increased precipitation over equatorial South America.
384 Annual mean river runoff for the Amazon River is simulated at 305, 297, and 308 km³/month for
385 LtoG_M0, LtoG_M1 and LtoG_M2, respectively, a slight improvement to the original
386 Preindustrial (PI) run runoff of 280 km³/month with using the standard present-day land cover
387 boundary condition. Compared to observations, ModelE2.1 shows a substantial deficit in
388 Amazon River runoff in present-day simulations because of insufficient precipitation over the
389 watershed (Fekete et al., 2001; Kelley et al., 2020).

390
391 Based on this evaluation of the different ways of translating LPJ PFTs to GISS PFTs, we found
392 that LtoG_M2 was the scheme that simulates global precipitation and surface temperature most
393 consistent with observations, and ground albedo that is closest to the standard pre-industrial
394 boundary conditions dataset used usually used to drive ModelE. Figure 3 shows the difference in
395 PFT cover fraction using LPJ-LMfire with the LtoG_M2 scheme compared to the standard
396 ModelE boundary condition land cover data set for the late preindustrial time (PI; 1850 CE).

397 Compared to the ModelE standard land cover dataset for PI, LPJ-LMfire simulates increased
 398 extent and fraction of most trees (drought broadleaf, evergreen needleleaf, and evergreen
 399 broadleaf). Despite selecting a relatively high threshold for tree height to be classified as shrubs
 400 (up to 11 meters for both arid and cold types) the simulated cover fraction of shrubs is low
 401 compared to the standard PI land cover dataset for ModelE. The coverage of both annual and
 402 perennial C₃ grasses is greater in LPJ-LMfire in extratropical and polar regions, similarly, C₄
 403 grasses, which are not present in cooler climates, shows greater coverage in LPJ-LMfire in
 404 equatorial regions. LPJ-LMfire simulates some vegetation cover in the Sahara and Arabian
 405 deserts while the standard PI boundary conditions dataset suggests that most of this region is
 406 bare soil.



407
 408 **Figure 3.** Differences between the LPJ-LMfire simulated vegetation distribution (PFTs and land
 409 cover type) and satellite-based land cover boundary conditions used in ModelE for PI control
 410 period and the selected mapping schemes (LtoG_M2).

411

412 **3.3 Vegetation Cover Changes under various combinations**

413 We chose a set of five model configurations (Table 2) to quantify the model bias and interannual
414 variability in our asynchronous coupling framework for the 2.5ka period. Figures S2.A, S2.B,
415 S2.C, S2D, and S2.E show the spatial differences between prescribed land cover boundary
416 conditions maps and land cover interactively simulated by our LPJ-LMfire-ModelE coupled
417 model, which is henceforth referred to as the “coupled model system”. These land cover
418 difference maps are shown for each of the different model configurations described above,
419 following the final iteration of the asynchronous coupling when the coupled model system is
420 assumed to be either equilibrated or the process was truncated due to instability (Table 2).
421 Figures S2.A, S2.B, and S2.C show the changes in the land cover from the default ModelE land
422 cover boundary conditions map for PI (Fig S1.A); Figures S2.D and S2.E show the differences
423 calculated from the modified vegetation following the PMIP4 protocols (Fig S1.B).

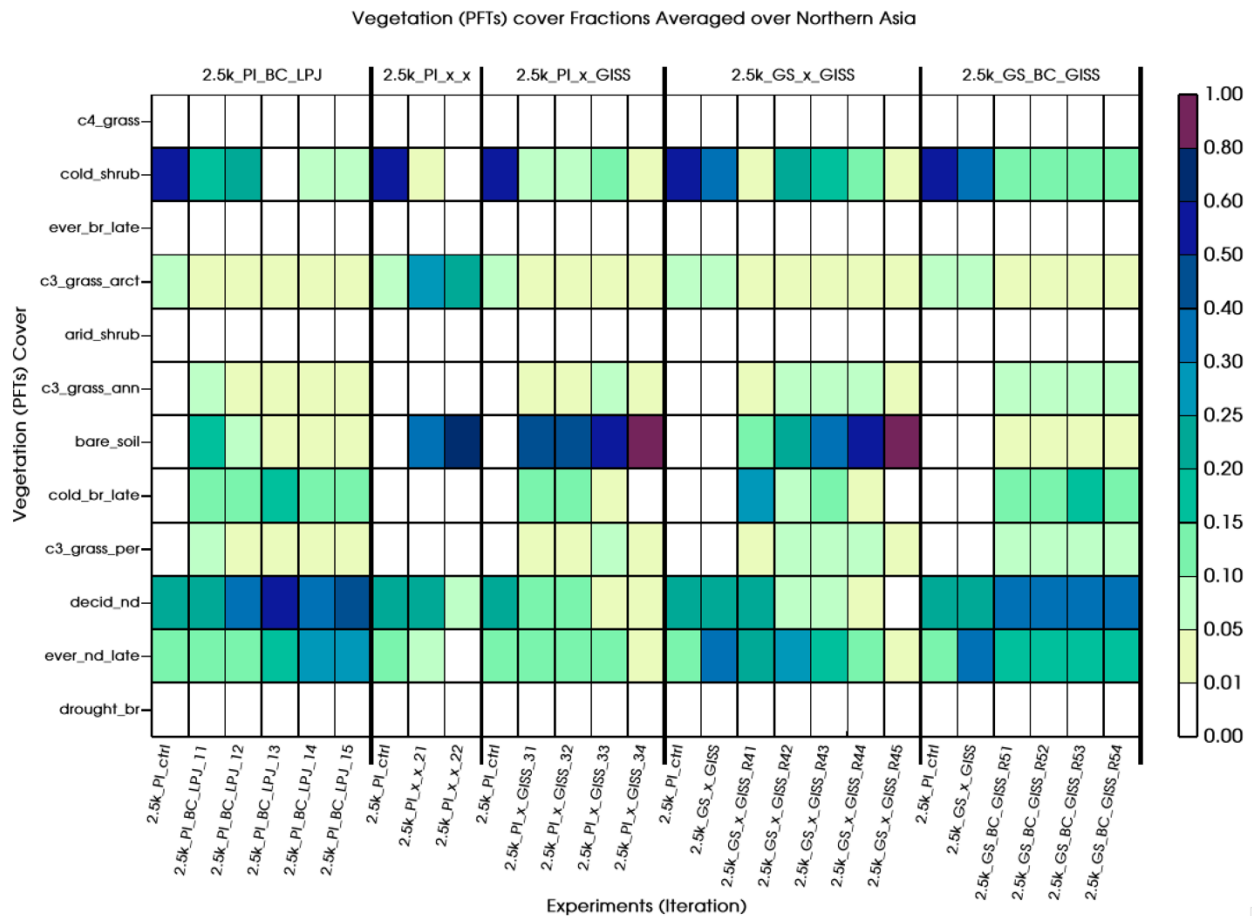
424

425 Across all configurations, most of the tree PFTs show an increase in cover in the coupled model
426 system relative to the prescribed land cover maps. However, in simulations where bias correction
427 to the climate model was not applied, deciduous needleleaf tree cover is reduced in the high
428 latitudes of the Northern Hemisphere (2.5k_PI_x_x, 2.5k_PI_x_GISS and 2.5k_GS_x_GISS)
429 and this, in turn, has a substantial impact on regional climate. The coupled model system
430 simulates increased annual and perennial C₃ grass cover across all configurations relative to the
431 prescribed maps, while the Arctic C₃ grass shows a mixed regional response. Increased C₄ grass
432 cover is mostly confined to the equatorial region and Southern Hemisphere; over the Northern
433 Hemisphere C₄ grass cover decreases, irrespective of the inclusion and exclusion of interannual
434 variability or bias correction. As discussed previously, the extent of arid and cold shrubs is
435 reduced significantly in the coupled model system relative to the prescribed maps, even when the
436 threshold height to separate trees shrubs was set at a relatively tall limit of 11 m. A similar
437 reduction in shrub cover relative to the land cover map used to initialize the simulation
438 vegetation distributions is also simulated under all configurations.

439

440 In Figures 4 and 5 we present heatmap-type diagrams of the mean land cover fraction over
441 selected regions to demonstrate and understand the pattern of change in vegetation distribution
442 simulated by the coupled model system. These figures depict changes in land cover under the

443 different asynchronous coupling experimental configurations used in this study. Vegetation
 444 fraction changes averaged over northern Asia (NAS) (Fig. 4) and eastern Africa (Fig. 5; see Fig.
 445 13 for the region boundaries; NAS: magenta; EAF: blue). Deciduous needleleaf tree cover over
 446 northern Asia (60°N-77°N, 70°E-135°E) is replaced by bare soil in all experimental
 447 configurations where bias correction of the climate model output was not applied. A similar
 448 disappearance of evergreen needleleaf late-successional forests, as well as a quick disappearance
 449 (within the first iteration) of cold shrubs, was also noticed. This suggests that, in the absence of
 450 bias correction the model's drift towards colder conditions strongly influences vegetation growth
 451 in subsequent iterations over higher latitudes, which is inconsistent with the standard land cover
 452 boundary condition dataset used with ModelE (Kelley et al., 2020). On the other hand, when bias
 453 correction is applied along with interannual variability from either model (2.5K_PI_BC_LPJ and
 454 2.5K_GS_BC_GISS), boreal forests are present in the northern Asia region along with cold
 455 shrubs and grasses.
 456

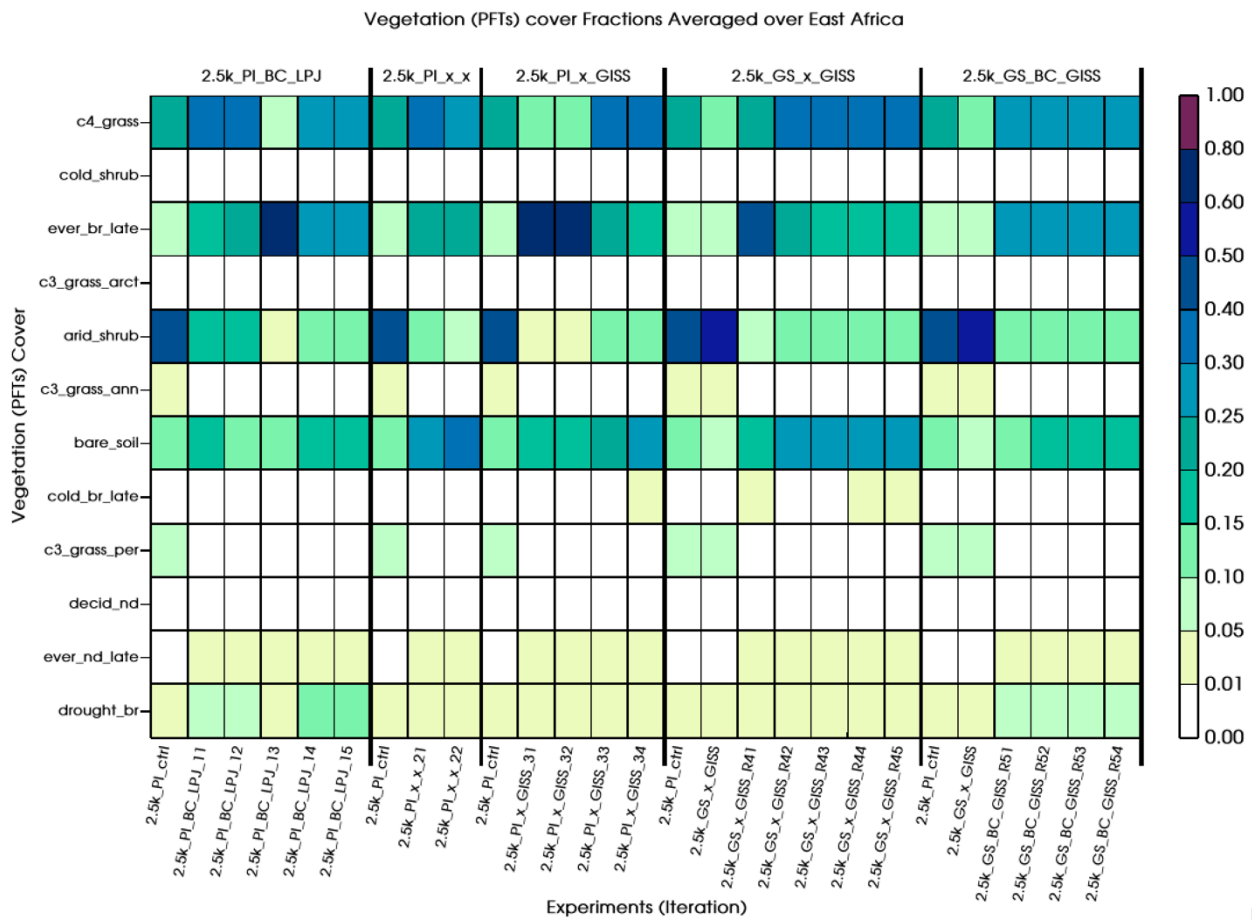


458 Figure 4. Area average of fractional land cover over Northern Asia region (60°N-77°N, 70°E-
 459 135°E) under the range of experimental configurations used in this study.

460

461 Over eastern Africa (EAF: 0° N-18° N, 25° E-46° E) the impact of bias correction is less
 462 important than over the high latitudes of the Northern Hemisphere. The presence of broadleaf
 463 tree PFTs (drought broadleaf and evergreen broadleaf) and C₄ grasses is consistent across all the
 464 experimental configurations we used. However, the cover fraction arid shrubs decreased
 465 substantially, associated with a slight increase in the bare soil fraction.

466



467

468 Figure 5. Same as Figure 4A, but for Eastern Africa (0°N-18°N, 25°E-46°E).

469

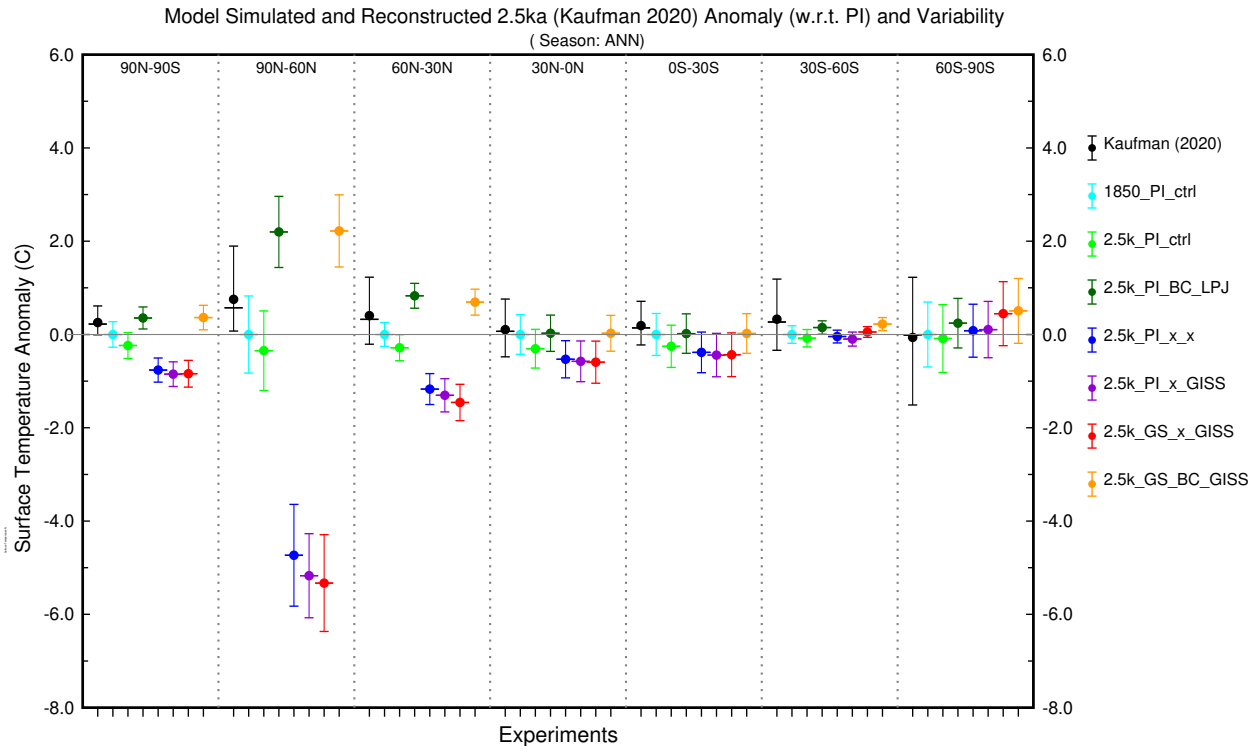
470 4.0 Comparison with paleoclimate-proxy records for 2.5ka

471 To evaluate the coupled model system's skill in representing past climate, we compared our
472 simulations for 2.5ka with multiproxy temperature reconstructions and speleothem-based oxygen
473 isotope records.

474

475 4.1 Comparisons with reconstructed temperature

476 Kaufman et al. (2020) used five different statistical methods to reconstruct temperature at 1319
477 globally distributed sites covering part or all of Holocene from a range of proxy types. For each
478 method, a 500-member ensemble of plausible reconstructions was presented. For comparison
479 with our model output, we extracted temperature anomalies for 2.5ka (relative to the value
480 reconstructed for the late preindustrial Holocene) from the ensemble reconstructions which we
481 binned into six latitude bands between the North and South Poles (each 30 degrees wide). We
482 computed the mean and median zonal anomaly using all 500 estimates of mean surface
483 temperature (MST) over each band for each of the five methodologies (total 2500), along with
484 the 5-95 percentile interval to represent uncertainty/variability among the sites in the zone and
485 across reconstruction methods (black bar in Figure 6) as suggested (Kaufman et al. 2020).



486

487 Figure 6: Comparison of model-simulated annual surface temperature anomalies and interannual
488 variability for 2.5ka (with LPJ-LMfire vegetation) against the independent proxy-based
489 temperature reconstructions (black, Kaufman et al., 2020). Mean (circle), median (line) along with
490 5-95 percentile range as variability bars (whiskers) and different colors represent the final iteration
491 of our different experiments.

492

493 It shows that the 2.5ka control simulation with present-day vegetation is comparable to pre-
494 industrial conditions (1850_PI_ctrl), exhibiting a slightly cooler climate. In contrast, proxy-based
495 surface temperature reconstructions (Kaufman et al., 2020) indicate slightly warmer conditions at
496 global mean as well as across most latitude bands, except the far south (60S-90S). Applying bias
497 correction allows the model to reproduce the same anomaly sign as the reconstruction, with
498 minimal global (90N-90S) mean bias relative to the proxy data (2.5k_PI_BC_LPJ and
499 2.5k_GS_BC_GISS). Although the magnitude of warming remains higher at the northern
500 hemisphere high latitudes, this framework demonstrates the improved capability of the model to
501 reproduce reconstructions via incorporating biogeophysical effects of past vegetation by
502 adopting a bias correction. Model simulations where bias correction was not applied show colder
503 conditions than the reconstructions globally and in the Northern Hemisphere. These differences
504 between model and proxy are very large in the high latitudes of the Northern Hemisphere and
505 statistically significant throughout the extra-tropics. In the Southern Hemisphere, the differences
506 between model and proxy reconstructions are smaller and insignificant, and there is less
507 difference between simulations with and without bias correction. It should be noted that the
508 larger uncertainty in reconstructed temperature over the southern polar band is due to a
509 noticeably lower number of available proxy records (157 records; Kaufman et al., 2020).

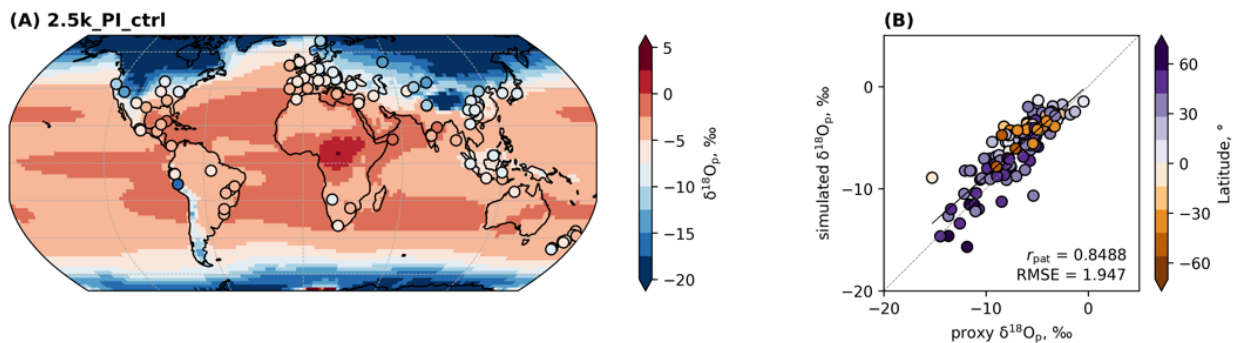
510

511 **4.2 Comparisons with speleothem oxygen isotope ratios**

512 The isotopic composition of oxygen in water, expressed as the ratio of ^{18}O to ^{16}O serves as a
513 fundamental tracer for investigating changes in the hydrological cycle. This ratio is highly
514 sensitive to regional climate conditions and to the processes that regulate the hydrological cycle,
515 such as temperature, precipitation, and evaporation. ModelE2.1 includes a representation of the
516 stable water isotopologues as passive tracers and the isotopic composition of precipitation can be
517 diagnosed from the model output (Aleinov and Schmidt, 2006; LeGrande and Schmidt, 2006;

518 Schmidt, 1998). We compared the simulated mean annual isotopic composition of precipitation
 519 ($\delta^{18}\text{O}_p$) with oxygen isotope records from the Speleothem Isotope Synthesis and Analysis
 520 (SISAL) version 2 database (Comas-Bru et al., 2020). Using the published chronologies for each
 521 speleothem record we extracted all samples dated between 3-2 ka, which resulted in 163
 522 measurements from 111 sites. Depending on their mineralogy (i.e., calcite or aragonite), the
 523 mean $\delta^{18}\text{O}$ values (VPDB) were converted to their drip water equivalents that could be compared
 524 to simulated $\delta^{18}\text{O}_p$ (VSMOW) (Comas-Bru et al., 2020). We used simulated mean surface air
 525 temperature obtained from the grid points nearest each cave sites to estimate the cave
 526 temperature required to convert mineral $\delta^{18}\text{O}$ to an equivalent the drip water value. For each of
 527 our model experiments, we extracted simulated $\delta^{18}\text{O}_p$ nearest to each cave site and compared it
 528 with the estimated drip-water $\delta^{18}\text{O}$.

529 Overall, the mean $\delta^{18}\text{O}_p$ spatial distribution in all 2.5ka simulations is in excellent agreement
 530 with the proxies, showing better pattern correlations (r_{pat}) than 0.83 (Figure 7), with
 531 the 2.5k_PI_x_x iteration marginally showing the highest skill (i.e., $r_{pat} = 0.85$ and RMSE =
 532 1.90; shown in supplementary Fig S4). For comparison, the worst simulation using this metric,
 533 2.5k_GS_BC_GISS, is almost as equally skillful ($r_{pat} = 0.84$ and RMSE = 1.92; Fig. S4),
 534 demonstrating that none of the different configurations we presented here were significantly
 535 different.



536

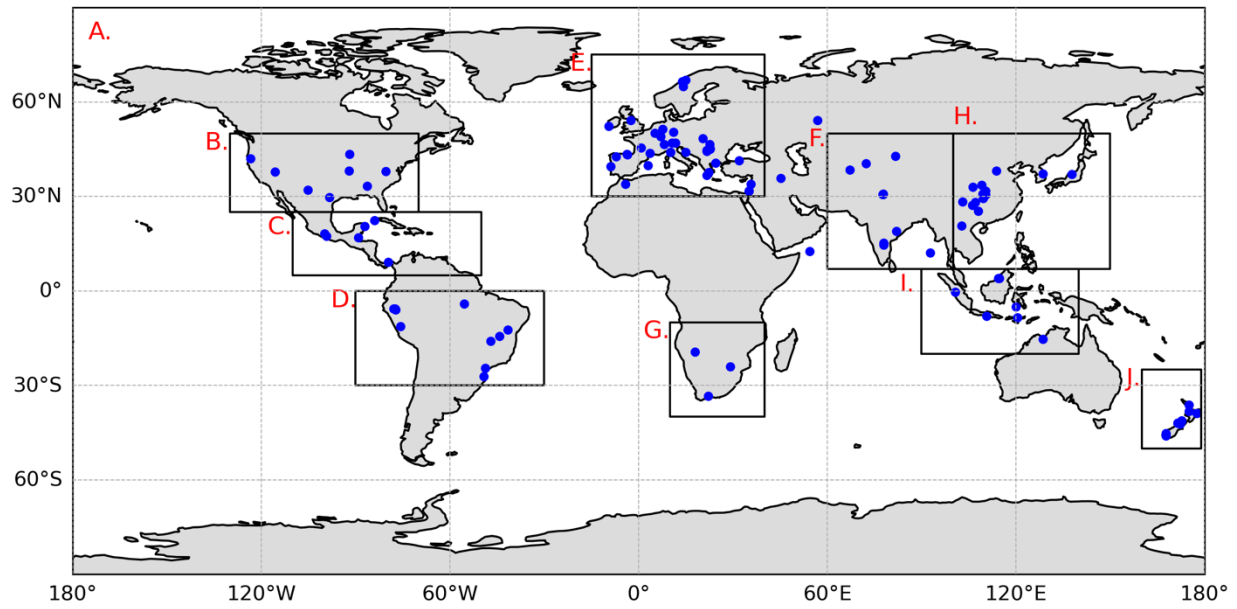
537 Figure 7. Comparison of simulated $\delta^{18}\text{O}_p$ with speleothem $\delta^{18}\text{O}$. Left: global distribution (70° S-
 538 70° N) of simulated $\delta^{18}\text{O}_p$ (background) and speleothem $\delta^{18}\text{O}$ (circles), converted to their drip
 539 water equivalents (see text) for the 2.5k_PI_ctrl simulation. Right: scatterplots between simulated
 540 and proxy $\delta^{18}\text{O}_p$. Black line represents the least squares regression fits to data points while the gray
 541 dashed line represents the 1:1 line. r_{pat} and RMSE are reported in the lower right corner of the
 542 scatterplot. For comparison against each model experiment, see Fig. S4

543

544 Regionally, we similarly found that most simulations show no significant deviation with each
545 other (Figure 8, Figure 9). We note, however, that over Europe (Figure 9E), variability may be
546 explained by the observed change in magnitude on both SAT and summer precipitation among
547 simulations (further sections). Over India and Central Asia (Figure 9F), simulations with bias
548 correction show lower correlation and higher RMSE values compared to other models against
549 proxy $\delta^{18}\text{O}_p$. This is likely related to the observed increase in mean summer precipitation over
550 this region that were not reflected in the proxy sites.

551

552 Compared to proxy $\delta^{18}\text{O}_p$, simulations over certain regions show better agreement. Europe,
553 which is the most densely sampled region, show the best agreement with the proxies (i.e., high
554 correlation, closest to the reference point, Figure 9E) with the 2.5k_PI_x_GISS iteration best
555 capturing the spatial $\delta^{18}\text{O}_p$ pattern (i.e., $r_{pat} = 0.94$ and $\text{RMSE} = 1.26$). In contrast, simulations
556 over Central America, South America and Africa show the least skill where the magnitude of
557 $\delta^{18}\text{O}_p$ change are consistently underestimated (i.e., moderate to high correlation but farthest away
558 from the reference point). This may largely be due to inadequate sampling in these regions,
559 especially for Africa, and/or both precipitation and SAT influencing $\delta^{18}\text{O}$ may be underestimated
560 at these proxy locations, resulting in a generally muted $\delta^{18}\text{O}$ response across simulations. Cave-
561 specific factors that alter speleothem $\delta^{18}\text{O}$ (e.g., groundwater mixing, fractionation, (Baker et al.,
562 2019; Hartmann and Baker, 2017; Lachniet, 2009) are also not effectively reproduced in the
563 models, contributing to the proxy-model mismatch. Regions where the largest simulated SAT,
564 precipitation, and $\delta^{18}\text{O}_p$ change relative to the 2.5k_PI_ctrl are observed, such as northern Africa,
565 the Amazon basin and Siberia, are not adequately represented by reconstructions, highlighting
566 the need to expand the proxy network to marine-based records and polar regions over the period
567 of interest to capture the full range of isotopic variation.

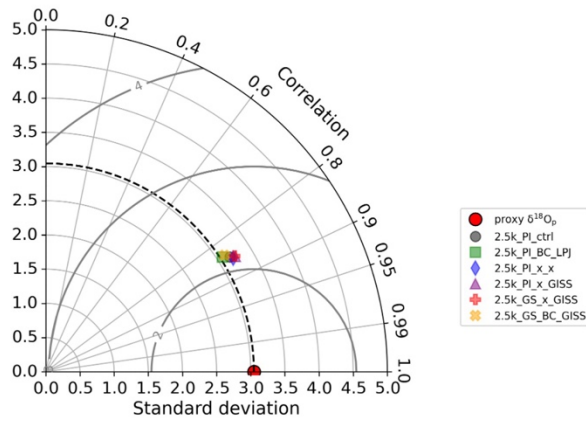


568

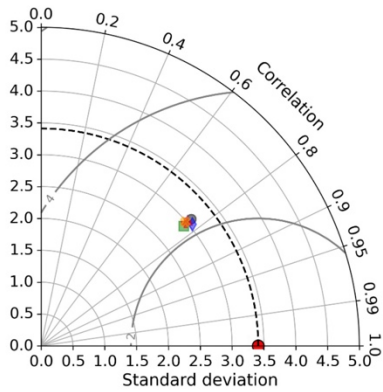
569 Figure 8. Demarcation of each geographical region. Labels A to J correspond to the respective

570 Taylor diagram plots in Figure 9.

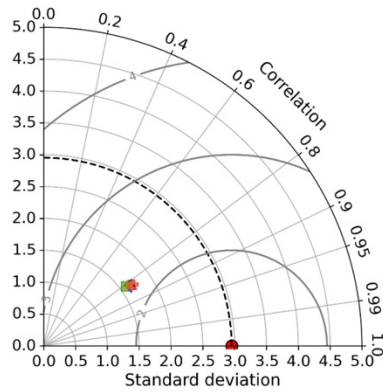
A. Global (n = 111)



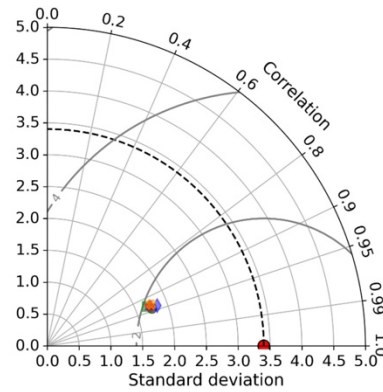
B. North America (n = 8)



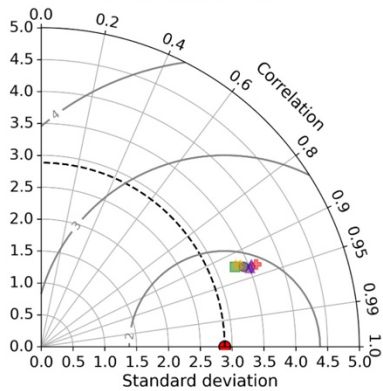
C. Central America (n = 6)



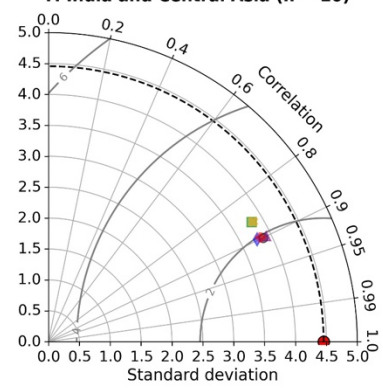
D. South America (n = 11)



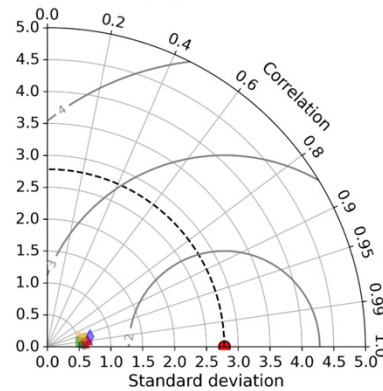
E. Europe (n = 33)



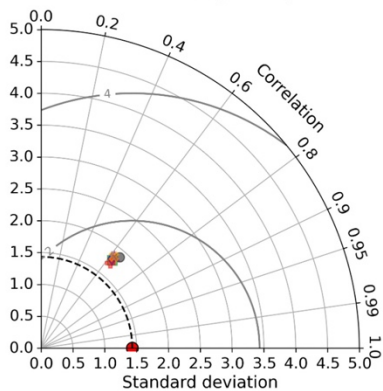
F. India and Central Asia (n = 10)



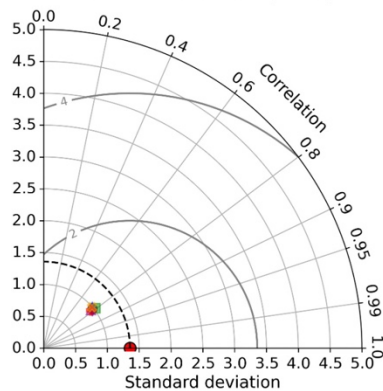
G. Africa (n = 3)



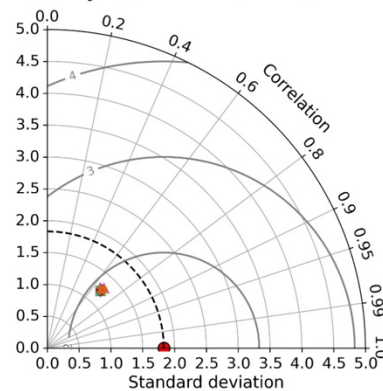
H. East Asia (n = 14)



I. Maritime Continent (n = 7)



J. New Zealand (n = 12)



572 Figure 9. Taylor diagrams showing the r , SD and RMSE values between the proxy-derived and
573 simulated $\delta^{18}\text{O}_p$ for each 2.5k iteration globally (A) and at each subregion (B to J). Subregions are
574 demarcated in supporting figure 8.

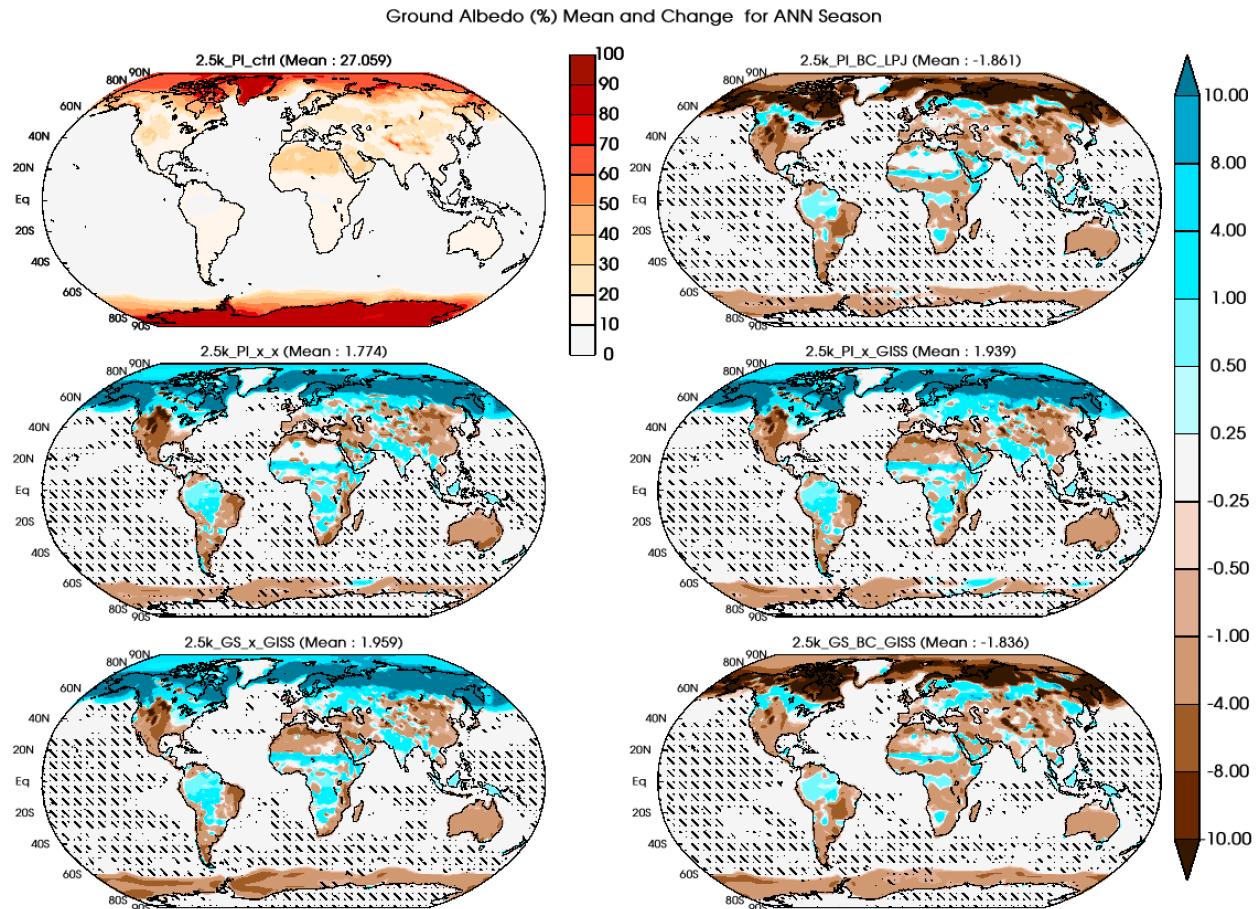
575

576

577 **5.0 Global climate response**

578 To evaluate the spatial features of the equilibrium climate simulated by ModelE, we analyzed the
579 last 100 years of the final iteration of each coupled model system experimental configuration. We
580 aimed to understand the biogeophysical feedback due to vegetation cover changes as well as the
581 role of model configuration on climate. Figure 10 shows surface albedo (%) for ModelE in its
582 initial PI state, and differences between this initial state and simulated albedo for 2.5ka using the
583 coupled model system. We used student's t-tests to estimate if the albedo differences were
584 statistically significant at 95% confidence interval. The coupled model system shows substantial
585 vegetation cover change over the high latitudes of the Northern Hemisphere. As expected, most of
586 the significant changes occur over land, while changes in albedo over the oceans are largely
587 insignificant. The spatial pattern of albedo change differs between simulations where bias
588 correction was applied (2.5k_PI_BC_LPJ and 2.5k_GS_BC_GISS) and those where it was not
589 (2.5k_PI_x_x, 2.5k_PI_x_GISS, and 2.5k_GS_x_GISS). Albedo over the high latitudes of the
590 Northern Hemisphere decreases up to 10% caused by increased tree cover fraction (deciduous
591 needleleaf and evergreen needleleaf) in the coupled model system relative to standard PI land
592 cover dataset.

593



594

595 Figure 10. Annual mean (top left; 2.5k_PI_ctrl) and change (all other panels) of surface albedo
 596 (%) for the final iteration of various experiment configurations listed in Table 2. Stippling indicates
 597 the region over which change is not statistically significant at a 95% confidence interval (Used the
 598 student's t-test).

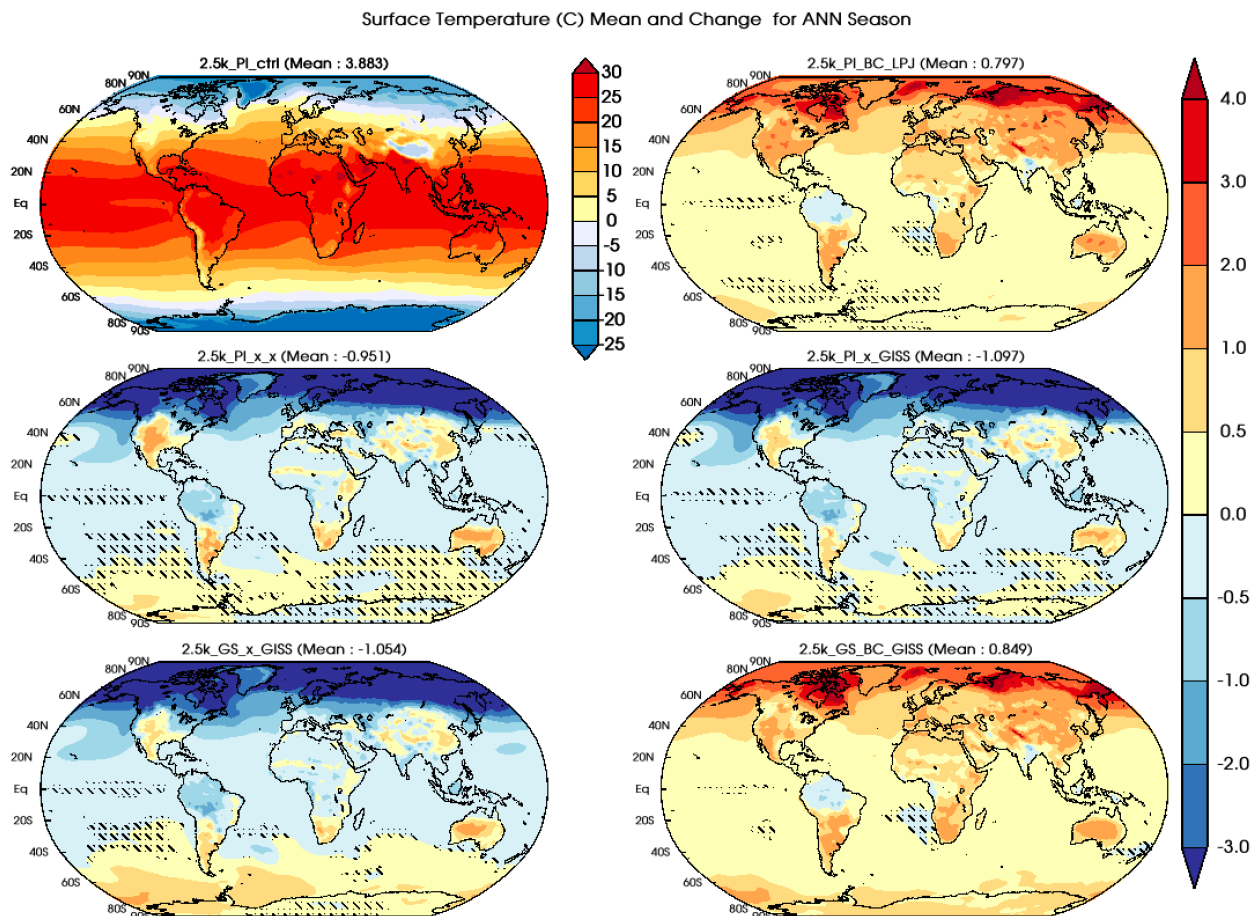
599

600 This increased tree cover fraction subsequently absorbs more incoming solar radiation and raises
 601 surface temperature by 2-4 °C over high latitude regions compared to the control run (Fig. 11
 602 top-right and bottom-right panels). In experiments where bias correction was not applied
 603 (2.5k_PI_x_x, 2.5k_PI_x_GISS and 2.5k_GS_x_GISS), the relatively cold conditions simulated
 604 by the coupled model system shows an opposite albedo-vegetation response (> 3 °C cooling over
 605 Northern Hemisphere high latitudes). This drift towards a colder climate in the absence of bias
 606 correction resulted in the continuous formation of sea ice that ultimately reaches the (shallow)
 607 seabed, effectively creating land ice and eliminating the ocean from the grid cell. In coupled
 608 model system experiments without bias correction, we terminated the iterative processes when

609 this freezing of the ocean to the seabed occurred, because this condition caused the model to
610 crash (2.5k_PI_x_x, 2.5k_PI_x_GISS, and 2.5k_GS_x_GISS).

611
612 At lower latitudes, albedo tends to show decreases relative to the standard boundary conditions
613 in all experiments, particularly over the forested areas of the equatorial regions and temperate
614 latitudes of the Northern Hemisphere. Over the northern Africa and the Indian subcontinent
615 changes in both albedo and surface temperature are more mixed. Albedo change in central and
616 northern Africa driven by a reduction in the area occupied by shrubs and an increase in bare soil
617 fraction. This pattern of increased albedo is more prevalent in simulations that were initialized
618 with Green Sahara land cover boundary conditions.

619



620
621 Figure 11. Same as figure 10 for Surface air temperature (°C) mean and change on an annual scale
622 (ANN season).

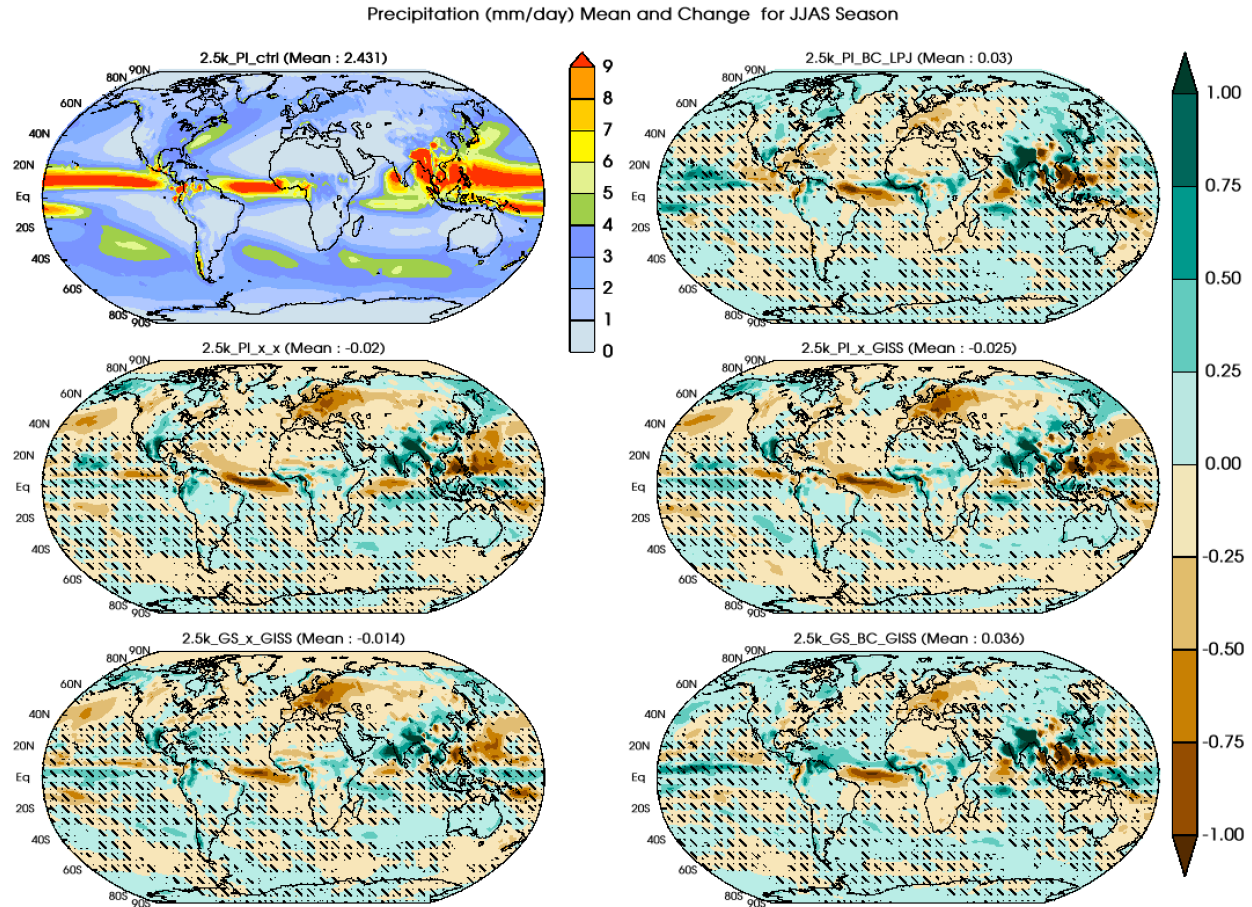
623

624 In experiments that were initialized with “Green Sahara” land cover boundary conditions where
625 interannual variability from GISS ModelE is included with and without adopting the bias
626 correction, comparison of the surface temperature response between simulations with
627 (2.5k_GS_x_GISS; Figure 11, bottom-left) and without bias correction (2.5k_GS_BC_GISS;
628 Figure 11, bottom-right) reveal the significance of bias correction for the asynchronous coupling
629 process. Broadly, we can observe that bias correction induces a warming of 0.7-0.8 °C, and
630 exclusion leads to a cooling of 0.9-1.1 °C, at the global scale, predominantly over the northern
631 hemisphere land regions.

632

633 Precipitation change across the model configurations is shown for Northern Hemisphere summer
634 (JJAS) at global scale in Figure 12. The significance of bias correction is noticeable over the
635 high latitudes of the Northern Hemisphere. Simulations with bias correction (2.5k_PI_BC_LPJ,
636 2.5k_GS_BC_GISS) lead to an increase in JJAS season precipitation relative to the initial
637 boundary conditions, while those experiments without bias correction (2.5k_PI_x_x,
638 2.5k_PI_x_GISS) show reductions in precipitation. Reductions in precipitation relative to initial
639 conditions are visible in Europe in all configurations and are greater in experiments where bias
640 correction was not applied. Another common feature among the experiments was the variable
641 spatial pattern of JJAS precipitation change over tropical regions. All configurations showed
642 increased precipitation over south and east Asia. Over the Nile headwaters in East Africa
643 (Melesse et al., 2011) precipitation increased, particularly in those experiments where bias
644 correction was applied. Interestingly, increased Northern Hemisphere summer monsoon
645 precipitation season (JJAS) over the Asian continent was simulated across all configurations. In
646 contrast, only a marginal northward procession of ITCZ over tropical Africa was simulated.

647



648

649

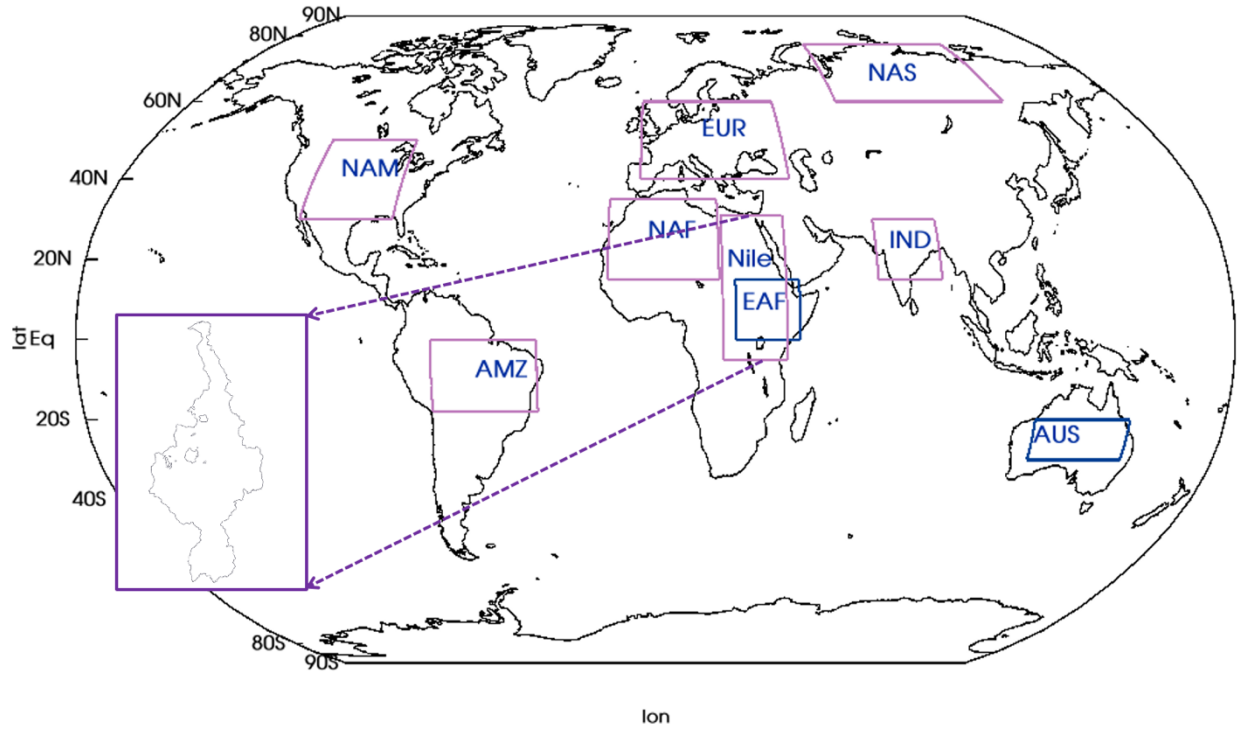
650 Figure 12. Same as figure 10 for precipitation (mm/day) mean and change for the JJAS season.

651

652 5.1 Regional climate

653 The spatial pattern of changes in climatic features for 2.5ka using our coupled model system
 654 shows several prominent and robust regional signatures of climate change. We selected nine
 655 regions over land (Fig. 13; Table 3) to analyze regional temperature and precipitation changes in
 656 our simulations. Area-averaged time-series anomalies with respect to the 2.5ka control run
 657 (2.5k_PI_ctrl) for the various experiments performed are calculated for these different regions.

658



659

660

661 Figure 13. Boundaries for the regions used for regional analysis. The inset map shows the Nile
 662 River basin in high resolution, which is superimposed upon the ModelE resolution to generate
 663 the grid-specific weights for the Nile River basin. The EAF and AUS regions are used in Figs. 4
 664 and 15.

665

666

667 **Table 3:** - Regions details including the boundary co-ordinates for all the regions.

| Region (long name) | Region (short name) | Region boundary (Latitudes) | Region boundary (Longitudes) |
|-------------------------------|--------------------------------|--|---|
| North America | NAM | 30°-50° N | 115°-85° W |
| Amazon Rainforest Region | AMZ | 0°-18° S | 37°-70° W |
| Northern Asia | NAS | 60°-77° N | 70°-135° E |
| North Africa | NAF | 15°-35° N | 15° W-20° E |
| Europe | EUR | 40°-60° N | 5° W-45° E |
| Indian Region | IND | 15°-30° N | 70°-90° E |
| Nile River Basin | Nile | 5° S-31° N | 21°-41° E |
| East Africa | EAF | 5°-15° N | 25°-45° E |
| Australia | AUS | 20°-30° S | 120°-150° E |

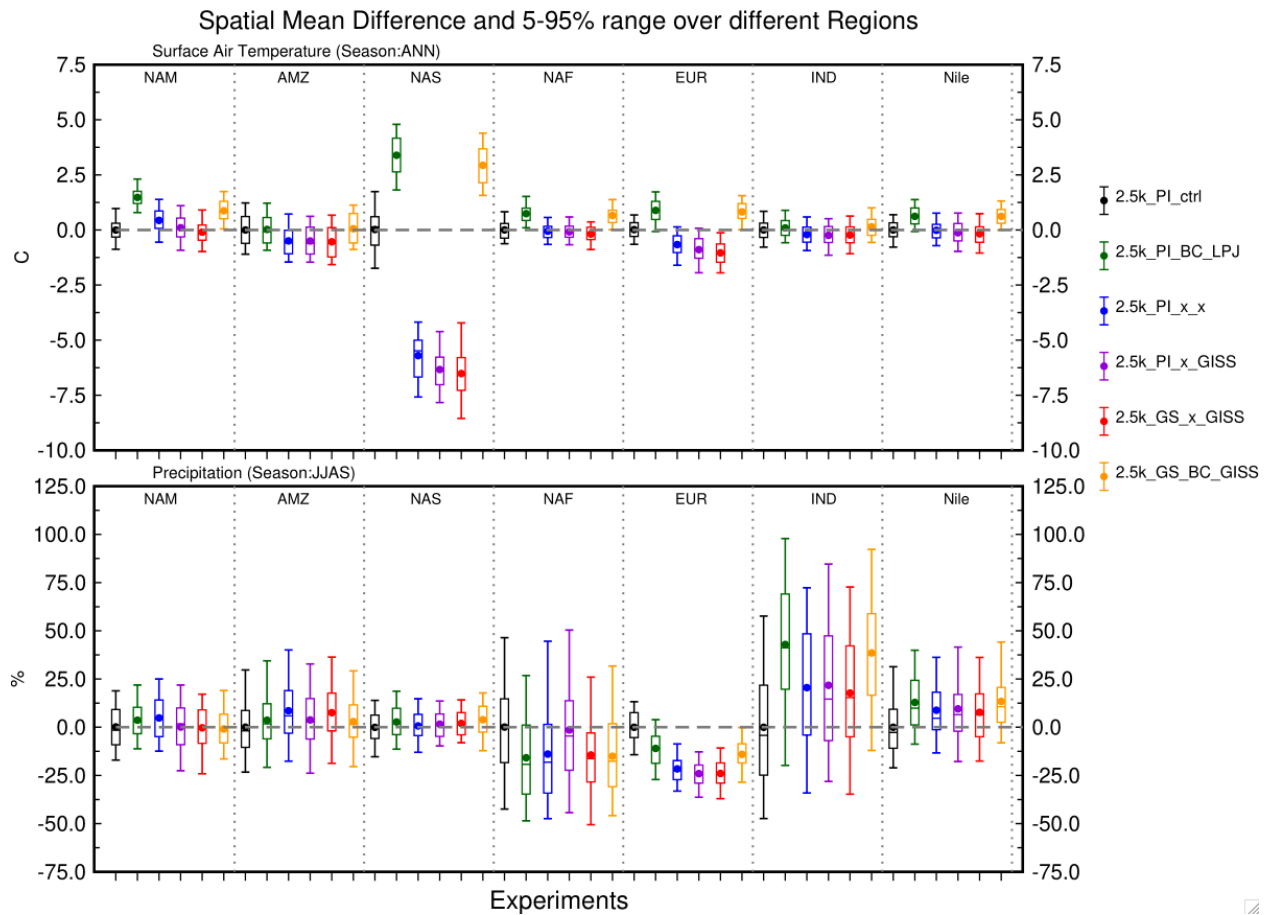
668

669

670 Figure 14 shows box-and-whisker plots of mean and median annual surface temperature (top)
 671 and JJAS seasonal precipitation (bottom) change, as well as the 5-95 percentile range
 672 (interannual variability) along with the upper and lower quartiles (25th and 75th percentiles) of the
 673 anomaly time series for each region. As suggested from the global analyses of spatial patterns,
 674 the shift towards relatively warmer or colder climate as a result of applying bias correction is
 675 evident. Bias correction leads to pronounced warming over northern Asia (NAS region) of 3-4
 676 °C, while without bias correction this region cools by 5-6 °C. The partition between experiments
 677 with and without bias correction is also apparent over selected regions of the mid-latitudes
 678 between 35°-60° N (NAS and EUP).

679

680 Except for northern Asia (NAS), all regions show approximately similar interannual variability
 681 in mean annual surface temperature. In northern Asia interannual variability is greater, especially
 682 in simulations where bias correction was not applied. Our results show that interannual
 683 variability in summer temperature in northern Asia is sensitive to changes in land cover, with
 684 greater variability in simulations where bias correction was not applied.



686

687 Figure 14. Regional change in surface air temperature (top panel, °C, annual mean) and
 688 precipitation (bottom panel, %, JJAS) for the various simulations with respect to the 2.5ka control
 689 run (2.5k_PI_ctrl). Regions name as listed in table 3.

690

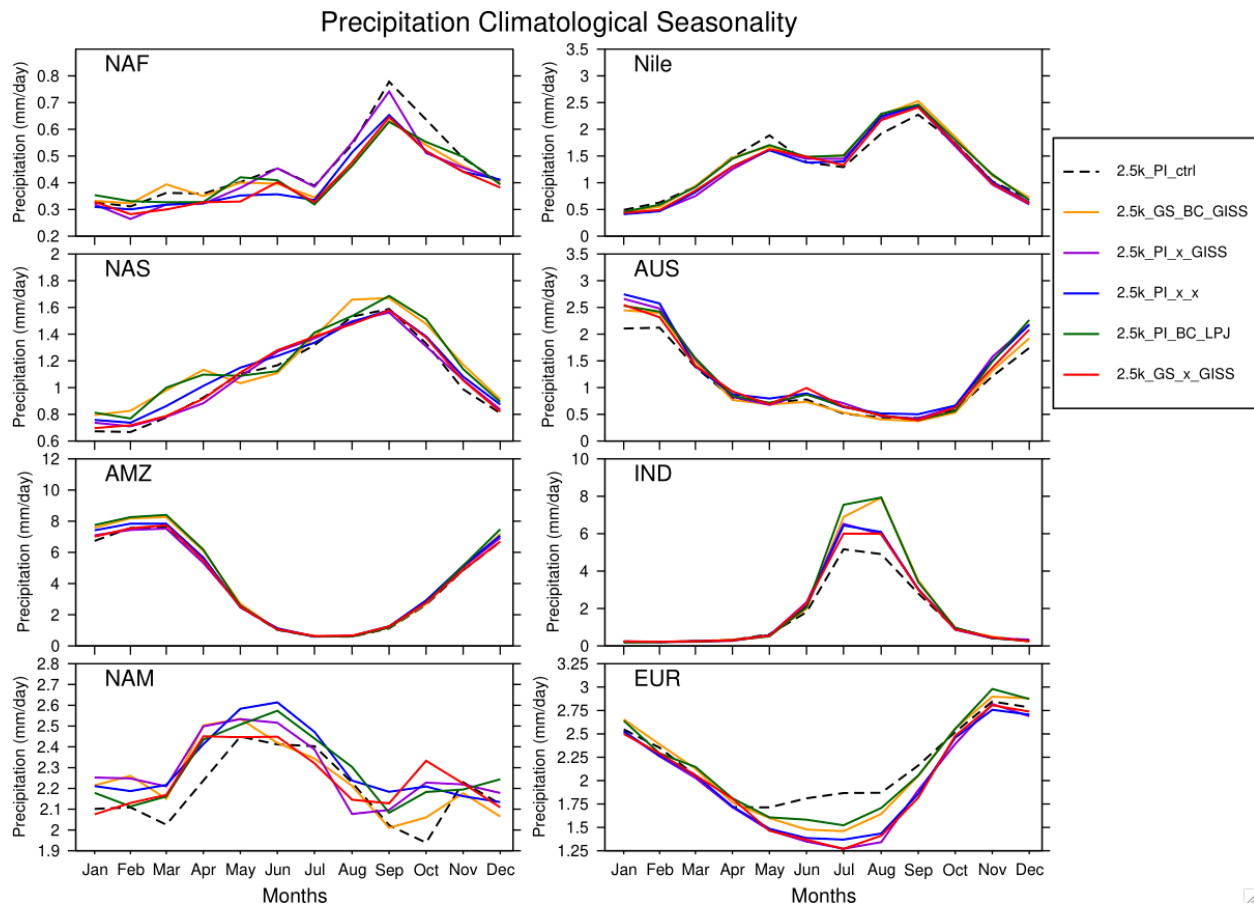
691 Simulated 2.5ka precipitation for the Northern Hemisphere summer (JJAS) shows substantial
 692 changes in mean state relative to the 2.5ka control with PI vegetations, particularly for the
 693 tropical regions of northern Africa, India, and the Nile basin (Fig. 14, bottom panel). Interannual
 694 variability in precipitation is comparable to the initial control run (black line). However, the
 695 magnitude of variability differs across the regions; it is more prominent in tropical regions than
 696 in the extratropic. An increase in mean precipitation of order of 20-30% without bias correction
 697 and up to 40% with bias correction is simulated in JJAS season precipitation for the Indian
 698 summer monsoon region (IND and it is in a range of 10-25% increase over the Nile basin region.
 699 A drying pattern over Europe (EUR) ranges from 10-25% and is consistent for all the

700 simulations; a greater decrease in European precipitation was simulated when bias correction is
701 not adopted. A similar drying pattern was also simulated over the North America (NAM) and
702 northern Africa (NAF) regions. The relatively small magnitude of interannual variability in
703 precipitation over Europe and North America suggests that model does not produce high
704 variability across these regions and that it is not sensitive to the different experimental
705 configurations. Despite the large changes in both mean state and variability in temperature,
706 precipitation over northern Asia (NAS) changes little from the control state and across
707 simulations. In the Amazon region (AMZ), precipitation changes were small and not
708 significantly different between simulations. Without bias correction, the coupled model system
709 suggests a modest increase in mean seasonal precipitation up to 10%. We also noticed a similar
710 response of slightly increased precipitation in Southern Hemisphere summer (DJF) over
711 Australia (not shown here).

712

713 We further investigated the way our experiments influenced the seasonal cycle of temperature
714 and precipitation over the regions discussed above. Our results show that the seasonal cycle of
715 surface temperature is broadly similar across experiments for all the equatorial regions except the
716 Amazon (AMZ) region, where surface temperature is reduced by 0.5 °C in experiments where
717 bias correction was not applied (Fig. S3). Over the northern Asia (NAS) region, we see a
718 considerable difference in the seasonal cycle of temperature of 5-15 °C between runs with and
719 without bias correction. The seasonal cycle of temperature in the 2.5ka control (2.5k_PI_ctrl)
720 simulation over NAS is intermediate to the experiments but tracks closer to the simulations
721 where bias correction was applied, particularly in Northern Hemisphere winter, where, as noted
722 above, simulations without bias correction result in very cold conditions in this region.

723



724
 725 Figure 15. Seasonality of precipitation averaged over the selected regions for the final iteration of
 726 each experiment listed in table 2.

727
 728 Compared to temperature, the seasonal cycle of precipitation shows greater differences among
 729 simulations over several of the regions (Fig. 15). An increase of 2-3 mm/day over the Indian
 730 region (IND) is simulated during the Indian Summer Monsoon months (JJAS) when using LPJ-
 731 LMfire-generated land cover for both types of experiments (with and without bias correction),
 732 with the bias-corrected simulations showing a larger increase in precipitation than the non-bias-
 733 corrected ones. When bias correction is applied, the seasonal peak of precipitation shifts from
 734 July to August. Over Europe, we observe a decrease of up to 0.5 mm/day in summer
 735 precipitation relative to the control simulation in all simulations that use the LPJ-LMfire PFTs.
 736 Precipitation decreases even more when the bias correction was not applied. The North Africa
 737 region (NAF) also shows a slight decrease in precipitation relative to the control over most of the
 738 seasonal cycle, while in North America (NAM) we see an increase in precipitation outside of the
 739 JJAS summer months. The Amazon rainforest region (AMZ) shows no change in the seasonal

740 cycle of precipitation in all experiments. The Nile River basin (Nile) and Australian (AUS)
741 regions also show small increases in precipitation relative to the control in their respective
742 monsoon seasons (JJAS and DJF). Overall, the changes in annual precipitation cycle (increases
743 or decreases) over the regions are primarily driven by both the pole-equator thermal gradients in
744 the various experiments, as well as the biogeophysical effects associated with regional vegetation
745 changes over these regions (e.g. Indian Summer monsoon, North American and European
746 region) (Pausata et al., 2014; Tiwari et al., 2023; Singh et al., 2023).

747

748 **6.0 Discussion and Conclusions**

749 Here we presented a generalized technical framework for asynchronously coupling a climate
750 model (NASA GISS ModelE2.1) with a dynamic vegetation model (LPJ-LMfire) i.e., the “coupled
751 model system”, and demonstrate its skill in reconstructing climate in the late preindustrial
752 Holocene and for 2.5ka. We examined the role of bias and interannual variability corrections in
753 this process, and showed how they influence simulated land cover and climate. We demonstrated
754 the importance of considering such metrics in such a framework in our experimental design and
755 global and regional scale analyses. We performed a detailed evaluation and comparison of the
756 climate simulated by the coupled model system with reconstructions of air temperature (Kaufman
757 et al., 2020) and the isotopic composition of precipitation ($\delta^{18}\text{O}_p$) based on speleothems (Comas-
758 Bru et al., 2020). Similarly to previous studies that used asynchronous coupling to simulate
759 regional and global paleoclimate (Claussen*, 2009; Kjellstroem et al., 2009; de Noblet et al., 1996;
760 Strandberg et al., 2011, 2014b; Texier et al., 1997; Velasquez et al., 2021), we assessed the
761 influence of the biogeophysical feedback between land and atmosphere.

762 Our results demonstrate the pronounced influence of including bias correction when passing
763 simulated climate to the land surface model. To correct biases inherent in the climate model, in
764 selected experiments we passed climate anomalies relative to a control simulation to the land
765 model that were added to a standard baseline climatology based on contemporary observations. In
766 simulations without this bias correction, raw simulated climate was passed directly from ModelE
767 to LPJ-LMfire. Where bias correction was applied ModelE drifts towards warmer climate;
768 simulations without bias correction drift towards colder climate. This effect was especially
769 apparent in the high latitudes of the Northern Hemisphere, particularly over Asia. With bias
770 correction, high latitude vegetation is dominated by tree plant functional types, while without it,

771 cold shrubs and arctic grasses are the predominant form of land cover. These results are
772 characteristic of the well-known vegetation-albedo feedback that is important at high latitudes
773 (Charney et al., 1977; Charney, 1975; Doughty et al., 2012, 2018; Pang et al., 2022; Stocker et al.,
774 2013; Swann et al., 2010; Zeng et al., 2021).

775

776 The effects of bias correction on precipitation were less apparent and confined to regional scale.
777 We simulated a greater Indian summer monsoon season (JJAS) precipitation with bias correction
778 (>1 mm/day), and a nominal increase of ~ 0.5 mm/day across east China, Africa, and the North
779 American monsoon region. In other regions, the patterns of precipitation change were similar
780 across all experiments except for Europe where drier conditions are simulated in summer (up to $-$
781 1 mm/day) in simulations where bias correction was not applied.

782

783 The high latitudes of the Northern Hemisphere were also the region with the largest disagreement
784 between model and independent, multi-proxy temperature reconstructions. These comparisons
785 also highlighted the important role of bias correction; experiments with correction were much more
786 similar to reconstructions than those without. Simulations of the isotopic composition of
787 precipitation ($\delta^{18}\text{O}_p$) shows an excellent agreement with speleothem records with a pattern
788 correlation greater than 0.8. However, the difference in the magnitude of model simulated $\delta^{18}\text{O}_p$
789 from proxies over various regions indicates an underestimation of relationship between surface
790 temperature and $\delta^{18}\text{O}_p$ variability (Henderson et al., 2006; Kurita et al., 2004). A global evaluation
791 of model skill is hindered by the difference in the number of independent paleoclimate
792 reconstructions available for different regions, particularly in north Asia where we see the greatest
793 sensitivity of the coupled model system to the experimental setup. When examining modeled and
794 reconstructed $\delta^{18}\text{O}_p$, in Europe, which is the region with the greatest number of records, we see a
795 robust pattern correlation with lower RMS values as compared to other regions.

796

797 In this study, we confirmed the importance of the land surface for simulating paleoclimate, even
798 for the late Holocene where land surface conditions were not as different from present as they were
799 during, e.g., the last glacial cycle or even mid-Holocene (6ka). We demonstrated that asynchronous
800 coupling can be a computationally inexpensive way of capturing land-atmosphere feedbacks and
801 improving the fidelity of the simulated climate. We noted that correcting bias present in the climate

802 model is essential for simulating climate that is consistent with independent reconstructions,
803 particularly for the high latitudes of the Northern Hemisphere. Future work with the coupled model
804 system will include quantification of the influence of major volcanic eruptions for regional and
805 global paleoclimate and the influence of past climate on the dynamics of complex civilizations in
806 prehistory.

807 **Code/Data availability**

808 Details to support the results in the manuscript is available as supplementary information is
809 provided with the manuscript. GISS Model code snapshots are available at
810 <https://simplex.giss.nasa.gov/snapshots/> (National Aeronautics and Space Administration, 2024),
811 LPJ-LMfire (<https://zenodo.org/records/5831747>), and important codes, calculated diagnostics as
812 well as other relevant details are available at zenodo repository
813 (<https://doi.org/10.5281/zenodo.13626434>) (Singh et al., 2024). However, raw model outputs data
814 and codes are available on request from author due to large data volume.

815

816 **Acknowledgements**

817 RS, KT, ANL and FL acknowledge support by the National Science Foundation under Grant No.
818 ICER-1824770. ANL acknowledges institutional support from NASA GISS. Resources
819 supporting this work were provided by the NASA High-End Computing (HEC) Program through
820 the NASA Center for Climate Simulation (NCCS) at Goddard Space Flight Center and from the
821 Department of Earth Sciences at The University of Hong Kong. The authors thank for their input
822 through multiple discussions the project members and collaborators of the ICER-1824770 project,
823 ‘Volcanism, Hydrology and Social Conflict: Lessons from Hellenistic and Roman-Era Egypt and
824 Mesopotamia’. RS and FL acknowledge additional support from European Research Council grant
825 agreement no. 951649 (4-OCEANS project).

826

827 **Author’s contributions**

828 RS, KT and ANL identified the study period in consultation with the other authors and RS, AK,
829 KT, ANL and JOK designed the asynchronous coupling framework. RS and AK implemented it
830 and performed the simulations using NASA GISS ModelE and LPJ-LMfire models. IA and RR
831 provided the essential technical support while implementing the framework. RS and RDR created
832 the figures in close collaboration with KT, ANL. RS wrote the first draft of the manuscript and

833 RDR, KT, ANL, and JOK led the writing of subsequent drafts. All authors contributed to the
834 interpretation of results and the drafting of the text.

835 **Competing interests**

836 The authors declare no competing interests.

837

838 **Short Summary**

839 This study presents and demonstrates an experimental framework for asynchronous land-
840 atmosphere coupling using the NASA GISS ModelE and LPJ-LMfire models for the 2.5ka period.

841 This framework addresses the limitation of NASA ModelE, which does not have a fully dynamic
842 vegetation model component. It also shows the role of model performance metrics, such as model
843 bias and variability, and the simulated climate is evaluated against the multi-proxy paleoclimate
844 reconstructions for the 2.5ka climate.

845

846 **References**

847 Aleinov, I. and Schmidt, G. A.: Water isotopes in the GISS ModelE land surface scheme, *Global*
848 *and Planetary Change*, 51, 108–120, <https://doi.org/10.1016/j.gloplacha.2005.12.010>, 2006.

849 Baker, A., Hartmann, A., Duan, W., Hankin, S., Comas-Bru, L., Cuthbert, M. O., Treble, P. C.,
850 Banner, J., Genty, D., Baldini, L. M., Bartolomé, M., Moreno, A., Pérez-Mejías, C., and Werner,
851 M.: Global analysis reveals climatic controls on the oxygen isotope composition of cave drip
852 water, *Nat Commun*, 10, 2984, <https://doi.org/10.1038/s41467-019-11027-w>, 2019.

853 Bauer, S. E., Tsigaridis, K., Faluvegi, G., Kelley, M., Lo, K. K., Miller, R. L., Nazarenko, L.,
854 Schmidt, G. A., and Wu, J.: Historical (1850–2014) Aerosol Evolution and Role on Climate
855 Forcing Using the GISS ModelE2.1 Contribution to CMIP6, *Journal of Advances in Modeling*
856 *Earth Systems*, 12, e2019MS001978, <https://doi.org/10.1029/2019MS001978>, 2020.

857 Berger, A., Loutre, M. F., and Mélice, J. L.: Equatorial insolation: from precession harmonics to
858 eccentricity frequencies, *Climate of the Past*, 2, 131–136, <https://doi.org/10.5194/cp-2-131-2006>,
859 2006.

860 Betts, R. A.: Offset of the potential carbon sink from boreal forestation by decreases in surface
861 albedo, *Nature*, 408, 187–190, <https://doi.org/10.1038/35041545>, 2000.

862 Bonan, G. B.: Forests and Climate Change: Forcings, Feedbacks, and the Climate Benefits of
863 Forests, *Science*, 320, 1444–1449, <https://doi.org/10.1126/science.1155121>, 2008.

864 Bonan, G. B., Pollard, D., and Thompson, S. L.: Effects of boreal forest vegetation on global
865 climate, *Nature*, 359, 716–718, <https://doi.org/10.1038/359716a0>, 1992.

- 866 Braconnot, P., Harrison, S. P., Kageyama, M., Bartlein, P. J., Masson-Delmotte, V., Abe-Ouchi,
867 A., Otto-Bliesner, B., and Zhao, Y.: Evaluation of climate models using palaeoclimatic data,
868 *Nature Clim Change*, 2, 417–424, <https://doi.org/10.1038/nclimate1456>, 2012.
- 869 Chandan, D. and Peltier, W. R.: African Humid Period Precipitation Sustained by Robust
870 Vegetation, Soil, and Lake Feedbacks, *Geophysical Research Letters*, 47, e2020GL088728,
871 <https://doi.org/10.1029/2020GL088728>, 2020.
- 872 Charney, J., Quirk, W. J., Chow, S., and Kornfield, J.: A Comparative Study of the Effects of
873 Albedo Change on Drought in Semi–Arid Regions, *Journal of the Atmospheric Sciences*, 34,
874 1366–1385, [https://doi.org/10.1175/1520-0469\(1977\)034<1366:ACSOTE>2.0.CO;2](https://doi.org/10.1175/1520-0469(1977)034<1366:ACSOTE>2.0.CO;2), 1977.
- 875 Charney, J. G.: Dynamics of deserts and drought in the Sahel, *Quarterly Journal of the Royal*
876 *Meteorological Society*, 101, 193–202, <https://doi.org/10.1002/qj.49710142802>, 1975.
- 877 Claussen, M.: Modeling bio-geophysical feedback in the African and Indian monsoon region,
878 *Climate Dynamics*, 13, 247–257, <https://doi.org/10.1007/s003820050164>, 1997.
- 879 Claussen*, M.: Late Quaternary vegetation-climate feedbacks, *Climate of the Past*, 5, 203–216,
880 <https://doi.org/10.5194/cp-5-203-2009>, 2009.
- 881 Collins, J. A., Prange, M., Caley, T., Gimeno, L., Beckmann, B., Mulitza, S., Skonieczny, C.,
882 Roche, D., and Schefuß, E.: Rapid termination of the African Humid Period triggered by
883 northern high-latitude cooling, *Nat Commun*, 8, 1372, [https://doi.org/10.1038/s41467-017-](https://doi.org/10.1038/s41467-017-01454-y)
884 01454-y, 2017.
- 885 Comas-Bru, L., Atsawawaranunt, K., Harrison, S., and members, S. working group: SISAL
886 (Speleothem Isotopes Synthesis and AnaLysis Working Group) database version 2.0,
887 <https://doi.org/10.17864/1947.256>, 2020.
- 888 Cox, P. M., Betts, R. A., Jones, C. D., Spall, S. A., and Totterdell, I. J.: Acceleration of global
889 warming due to carbon-cycle feedbacks in a coupled climate model, *Nature*, 408, 184–187,
890 <https://doi.org/10.1038/35041539>, 2000.
- 891 Dallmeyer, A., Claussen, M., Lorenz, S. J., Sigl, M., Toohey, M., and Herzschuh, U.: Holocene
892 vegetation transitions and their climatic drivers in MPI-ESM1.2, *Climate of the Past*, 17, 2481–
893 2513, <https://doi.org/10.5194/cp-17-2481-2021>, 2021.
- 894 Doherty, R., Kutzbach, J., Foley, J., and Pollard, D.: Fully coupled climate/dynamical vegetation
895 model simulations over Northern Africa during the mid-Holocene, *Climate Dynamics*, 16, 561–
896 573, <https://doi.org/10.1007/s003820000065>, 2000.
- 897 Doughty, C. E., Loarie, S. R., and Field, C. B.: Theoretical Impact of Changing Albedo on
898 Precipitation at the Southernmost Boundary of the ITCZ in South America, *Earth Interactions*,
899 16, 1–14, <https://doi.org/10.1175/2012EI422.1>, 2012.
- 900 Doughty, C. E., Santos-Andrade, P. E., Shenkin, A., Goldsmith, G. R., Bentley, L. P., Blonder,
901 B., Díaz, S., Salinas, N., Enquist, B. J., Martin, R. E., Asner, G. P., and Malhi, Y.: Tropical forest

902 leaves may darken in response to climate change, *Nat Ecol Evol*, 2, 1918–1924,
903 <https://doi.org/10.1038/s41559-018-0716-y>, 2018.

904 Eyring, V., Bony, S., Meehl, G. A., Senior, C. A., Stevens, B., Stouffer, R. J., and Taylor, K. E.:
905 Overview of the Coupled Model Intercomparison Project Phase 6 (CMIP6) experimental design
906 and organization, *Geoscientific Model Development*, 9, 1937–1958,
907 <https://doi.org/10.5194/gmd-9-1937-2016>, 2016.

908 Fekete, B. M., Vörösmarty, C. J., and Lammers, R. B.: Scaling gridded river networks for
909 macroscale hydrology: Development, analysis, and control of error, *Water Resources Research*,
910 37, 1955–1967, <https://doi.org/10.1029/2001WR900024>, 2001.

911 Gao, F., Morisette, J. T., Wolfe, R. E., Ederer, G., Pedelty, J., Masuoka, E., Myneni, R., Tan, B.,
912 and Nightingale, J.: An Algorithm to Produce Temporally and Spatially Continuous MODIS-
913 LAI Time Series, *IEEE Geoscience and Remote Sensing Letters*, 5, 60–64,
914 <https://doi.org/10.1109/LGRS.2007.907971>, 2008.

915 Hamilton, D. S., Hantson, S., Scott, C. E., Kaplan, J. O., Pringle, K. J., Nieradzik, L. P., Rap, A.,
916 Folberth, G. A., Spracklen, D. V., and Carslaw, K. S.: Reassessment of pre-industrial fire
917 emissions strongly affects anthropogenic aerosol forcing, *Nat Commun*, 9, 3182,
918 <https://doi.org/10.1038/s41467-018-05592-9>, 2018.

919 Harris, I., Osborn, T. J., Jones, P., and Lister, D.: Version 4 of the CRU TS monthly high-
920 resolution gridded multivariate climate dataset, *Sci Data*, 7, 109, <https://doi.org/10.1038/s41597-020-0453-3>, 2020.

922 Harrison, S. P., Bartlein, P. J., Izumi, K., Li, G., Annan, J., Hargreaves, J., Braconnot, P., and
923 Kageyama, M.: Evaluation of CMIP5 palaeo-simulations to improve climate projections, *Nature*
924 *Clim Change*, 5, 735–743, <https://doi.org/10.1038/nclimate2649>, 2015.

925 Hartmann, A. and Baker, A.: Modelling karst vadose zone hydrology and its relevance for
926 paleoclimate reconstruction, *Earth-Science Reviews*, 172, 178–192,
927 <https://doi.org/10.1016/j.earscirev.2017.08.001>, 2017.

928 Henderson, K., Laube, A., Gäggeler, H. W., Olivier, S., Papina, T., and Schwikowski, M.:
929 Temporal variations of accumulation and temperature during the past two centuries from
930 Belukha ice core, Siberian Altai, *Journal of Geophysical Research: Atmospheres*, 111,
931 <https://doi.org/10.1029/2005JD005819>, 2006.

932 Hoesly, R. M., Smith, S. J., Feng, L., Klimont, Z., Janssens-Maenhout, G., Pitkanen, T., Seibert,
933 J. J., Vu, L., Andres, R. J., Bolt, R. M., Bond, T. C., Dawidowski, L., Kholod, N., Kurokawa, J.,
934 Li, M., Liu, L., Lu, Z., Moura, M. C. P., O'Rourke, P. R., and Zhang, Q.: Historical (1750–2014)
935 anthropogenic emissions of reactive gases and aerosols from the Community Emissions Data
936 System (CEDS), *Geoscientific Model Development*, 11, 369–408, <https://doi.org/10.5194/gmd-11-369-2018>, 2018.

938 Ito, G., Romanou, A., Kiang, N. Y., Faluvegi, G., Aleinov, I., Ruedy, R., Russell, G., Lerner, P.,
939 Kelley, M., and Lo, K.: Global Carbon Cycle and Climate Feedbacks in the NASA GISS

- 940 ModelE2.1, *Journal of Advances in Modeling Earth Systems*, 12, e2019MS002030,
941 <https://doi.org/10.1029/2019MS002030>, 2020.
- 942 Jahn, B., Schneider, R. R., Müller, P.-J., Donner, B., and Röhl, U.: Response of tropical African
943 and East Atlantic climates to orbital forcing over the last 1.7 Ma, *Geological Society, London,*
944 *Special Publications*, 247, 65–84, <https://doi.org/10.1144/GSL.SP.2005.247.01.04>, 2005.
- 945 Kageyama, M., Braconnot, P., Harrison, S. P., Haywood, A. M., Jungclaus, J. H., Otto-Bliesner,
946 B. L., Peterschmitt, J.-Y., Abe-Ouchi, A., Albani, S., Bartlein, P. J., Brierley, C., Crucifix, M.,
947 Dolan, A., Fernandez-Donado, L., Fischer, H., Hopcroft, P. O., Ivanovic, R. F., Lambert, F.,
948 Lunt, D. J., Mahowald, N. M., Peltier, W. R., Phipps, S. J., Roche, D. M., Schmidt, G. A.,
949 Tarasov, L., Valdes, P. J., Zhang, Q., and Zhou, T.: The PMIP4 contribution to CMIP6 – Part 1:
950 Overview and over-arching analysis plan, *Geoscientific Model Development*, 11, 1033–1057,
951 <https://doi.org/10.5194/gmd-11-1033-2018>, 2018.
- 952 Kaplan, J. O., Krumhardt, K. M., and Zimmermann, N. E.: The effects of land use and climate
953 change on the carbon cycle of Europe over the past 500 years, *Global Change Biology*, 18, 902–
954 914, <https://doi.org/10.1111/j.1365-2486.2011.02580.x>, 2012.
- 955 Kaplan, J. O., Koch, A., and Vitali, R.: ARVE-Research/LPJ-LMfire: LPJ-LMfire (tropical
956 forest restoration), , <https://doi.org/10.5281/zenodo.5831747>, 2022.
- 957 Kattge, J., Díaz, S., Lavorel, S., Prentice, I. C., Leadley, P., Bönisch, G., Garnier, E., Westoby,
958 M., Reich, P. B., Wright, I. J., Cornelissen, J. H. C., Violle, C., Harrison, S. P., Van BODEGOM,
959 P. M., Reichstein, M., Enquist, B. J., Soudzilovskaia, N. A., Ackerly, D. D., Anand, M., Atkin,
960 O., Bahn, M., Baker, T. R., Baldocchi, D., Bekker, R., Blanco, C. C., Blonder, B., Bond, W. J.,
961 Bradstock, R., Bunker, D. E., Casanoves, F., Cavender-Bares, J., Chambers, J. Q., Chapin Iii, F.
962 S., Chave, J., Coomes, D., Cornwell, W. K., Craine, J. M., Dobrin, B. H., Duarte, L., Durka, W.,
963 Elser, J., Esser, G., Estiarte, M., Fagan, W. F., Fang, J., Fernández-Méndez, F., Fidelis, A.,
964 Finegan, B., Flores, O., Ford, H., Frank, D., Freschet, G. T., Fyllas, N. M., Gallagher, R. V.,
965 Green, W. A., Gutierrez, A. G., Hickler, T., Higgins, S. I., Hodgson, J. G., Jalili, A., Jansen, S.,
966 Joly, C. A., Kerckhoff, A. J., Kirkup, D., Kitajima, K., Kleyer, M., Klotz, S., Knops, J. M. H.,
967 Kramer, K., Kühn, I., Kurokawa, H., Laughlin, D., Lee, T. D., Leishman, M., Lens, F., Lenz, T.,
968 Lewis, S. L., Lloyd, J., Llusià, J., Louault, F., Ma, S., Mahecha, M. D., Manning, P., Massad, T.,
969 Medlyn, B. E., Messier, J., Moles, A. T., Müller, S. C., Nadrowski, K., Naeem, S., Niinemets,
970 Ü., Nöllert, S., Nüske, A., Ogaya, R., Oleksyn, J., Onipchenko, V. G., Onoda, Y., Ordoñez, J.,
971 Overbeck, G., et al.: TRY – a global database of plant traits, *Global Change Biology*, 17, 2905–
972 2935, <https://doi.org/10.1111/j.1365-2486.2011.02451.x>, 2011.
- 973 Kaufman, D., McKay, N., Routson, C., Erb, M., Dätwyler, C., Sommer, P. S., Heiri, O., and
974 Davis, B.: Holocene global mean surface temperature, a multi-method reconstruction approach,
975 *Sci Data*, 7, 201, <https://doi.org/10.1038/s41597-020-0530-7>, 2020.
- 976 Kelley, M., Schmidt, G. A., Nazarenko, L. S., Bauer, S. E., Ruedy, R., Russell, G. L., Ackerman,
977 A. S., Aleinov, I., Bauer, M., Bleck, R., Canuto, V., Cesana, G., Cheng, Y., Clune, T. L., Cook,
978 B. I., Cruz, C. A., Del Genio, A. D., Elsaesser, G. S., Faluvegi, G., Kiang, N. Y., Kim, D., Lacis,
979 A. A., Leboissetier, A., LeGrande, A. N., Lo, K. K., Marshall, J., Matthews, E. E., McDermid,

- 980 S., Mezuman, K., Miller, R. L., Murray, L. T., Oinas, V., Orbe, C., García-Pando, C. P.,
981 Perlwitz, J. P., Puma, M. J., Rind, D., Romanou, A., Shindell, D. T., Sun, S., Tausnev, N.,
982 Tsigaridis, K., Tselioudis, G., Weng, E., Wu, J., and Yao, M.-S.: GISS-E2.1: Configurations and
983 Climatology, *Journal of Advances in Modeling Earth Systems*, 12, e2019MS002025,
984 <https://doi.org/10.1029/2019MS002025>, 2020.
- 985 Kim, Y., Moorcroft, P. R., Aleinov, I., Puma, M. J., and Kiang, N. Y.: Variability of phenology
986 and fluxes of water and carbon with observed and simulated soil moisture in the Ent Terrestrial
987 Biosphere Model (Ent TBM version 1.0.1.0.0), *Geoscientific Model Development*, 8, 3837–
988 3865, <https://doi.org/10.5194/gmd-8-3837-2015>, 2015.
- 989 Kjellstroem, E., Strandberg, G., Brandefelt, J., Naeslund, J.-O., Smith, B., and Wohlfarth, B.:
990 Climate conditions in Sweden in a 100,000-year time perspective, 2009.
- 991 Köhler, P., Nehrbass-Ahles, C., Schmitt, J., Stocker, T. F., and Fischer, H.: A 156 kyr smoothed
992 history of the atmospheric greenhouse gases CO₂, CH₄, and N₂O and their radiative forcing,
993 *Earth System Science Data*, 9, 363–387, <https://doi.org/10.5194/essd-9-363-2017>, 2017.
- 994 Kubatzki, C. and Claussen, M.: Simulation of the global bio-geophysical interactions during the
995 Last Glacial Maximum, *Climate Dynamics*, 14, 461–471,
996 <https://doi.org/10.1007/s003820050234>, 1998.
- 997 Kurita, N., Yoshida, N., Inoue, G., and Chayanova, E. A.: Modern isotope climatology of Russia:
998 A first assessment, *Journal of Geophysical Research: Atmospheres*, 109,
999 <https://doi.org/10.1029/2003JD003404>, 2004.
- 1000 Lachniet, M. S.: Climatic and environmental controls on speleothem oxygen-isotope values,
1001 *Quaternary Science Reviews*, 28, 412–432, <https://doi.org/10.1016/j.quascirev.2008.10.021>,
1002 2009.
- 1003 Lamb, P. J.: Persistence of Subsaharan drought, *Nature*, 299, 46–48,
1004 <https://doi.org/10.1038/299046a0>, 1982.
- 1005 LeGrande, A. N. and Schmidt, G. A.: Global gridded data set of the oxygen isotopic composition
1006 in seawater, *Geophysical Research Letters*, 33, <https://doi.org/10.1029/2006GL026011>, 2006.
- 1007 Li, C.-F., Chytrý, M., Zelený, D., Chen, M.-Y., Chen, T.-Y., Chiou, C.-R., Hsia, Y.-J., Liu, H.-
1008 Y., Yang, S.-Z., Yeh, C.-L., Wang, J.-C., Yu, C.-F., Lai, Y.-J., Chao, W.-C., and Hsieh, C.-F.:
1009 Classification of Taiwan forest vegetation, *Applied Vegetation Science*, 16, 698–719,
1010 <https://doi.org/10.1111/avsc.12025>, 2013.
- 1011 Loulergue, L., Schilt, A., Spahni, R., Masson-Delmotte, V., Blunier, T., Lemieux, B., Barnola,
1012 J.-M., Raynaud, D., Stocker, T. F., and Chappellaz, J.: Orbital and millennial-scale features of
1013 atmospheric CH₄ over the past 800,000 years, *Nature*, 453, 383–386,
1014 <https://doi.org/10.1038/nature06950>, 2008.
- 1015 Ludlow, F. and Manning, J. G.: Volcanic Eruptions, Veiled Suns, and Nile Failure in Egyptian
1016 History: Integrating Hydroclimate into Understandings of Historical Change, in: *Climate Change*

- 1017 and Ancient Societies in Europe and the Near East: Diversity in Collapse and Resilience, edited
1018 by: Erdkamp, P., Manning, J. G., and Verboven, K., Springer International Publishing, Cham,
1019 301–320, https://doi.org/10.1007/978-3-030-81103-7_10, 2021.
- 1020 Magi, B. I.: Global Lightning Parameterization from CMIP5 Climate Model Output, *Journal of*
1021 *Atmospheric and Oceanic Technology*, 32, 434–452, <https://doi.org/10.1175/JTECH-D-13->
1022 00261.1, 2015.
- 1023 Manning, J. G., Ludlow, F., Stine, A. R., Boos, W. R., Sigl, M., and Marlon, J. R.: Volcanic
1024 suppression of Nile summer flooding triggers revolt and constrains interstate conflict in ancient
1025 Egypt, *Nat Commun*, 8, 900, <https://doi.org/10.1038/s41467-017-00957-y>, 2017.
- 1026 Mikhail, A.: Ottoman Iceland: A Climate History, *Environmental History*, 20, 262–284,
1027 <https://doi.org/10.1093/envhis/emv006>, 2015.
- 1028 Myneni, R. B., Hoffman, S., Knyazikhin, Y., Privette, J. L., Glassy, J., Tian, Y., Wang, Y., Song,
1029 X., Zhang, Y., Smith, G. R., Lotsch, A., Friedl, M., Morisette, J. T., Votava, P., Nemani, R. R.,
1030 and Running, S. W.: Global products of vegetation leaf area and fraction absorbed PAR from
1031 year one of MODIS data, *Remote Sensing of Environment*, 83, 214–231,
1032 [https://doi.org/10.1016/S0034-4257\(02\)00074-3](https://doi.org/10.1016/S0034-4257(02)00074-3), 2002.
- 1033 de Noblet, N., Braconnot, P., Joussaume, S., and Masson, V.: Sensitivity of simulated Asian and
1034 African summer monsoons to orbitally induced variations in insolation 126, 115 and 6 kBP,
1035 *Climate Dynamics*, 12, 589–603, <https://doi.org/10.1007/BF00216268>, 1996.
- 1036 Otto-Bliesner, B. L., Braconnot, P., Harrison, S. P., Lunt, D. J., Abe-Ouchi, A., Albani, S.,
1037 Bartlein, P. J., Capron, E., Carlson, A. E., Dutton, A., Fischer, H., Goelzer, H., Govin, A.,
1038 Haywood, A., Joos, F., LeGrande, A. N., Lipscomb, W. H., Lohmann, G., Mahowald, N.,
1039 Nehrbass-Ahles, C., Pausata, F. S. R., Peterschmitt, J.-Y., Phipps, S. J., Renssen, H., and Zhang,
1040 Q.: The PMIP4 contribution to CMIP6 – Part 2: Two interglacials, scientific objective and
1041 experimental design for Holocene and Last Interglacial simulations, *Geoscientific Model*
1042 *Development*, 10, 3979–4003, <https://doi.org/10.5194/gmd-10-3979-2017>, 2017.
- 1043 Pang, G., Chen, D., Wang, X., and Lai, H.-W.: Spatiotemporal variations of land surface albedo
1044 and associated influencing factors on the Tibetan Plateau, *Science of The Total Environment*,
1045 804, 150100, <https://doi.org/10.1016/j.scitotenv.2021.150100>, 2022.
- 1046 Pausata, F. S. R., Messori, G., and Zhang, Q.: Impacts of dust reduction on the northward
1047 expansion of the African monsoon during the Green Sahara period, *Earth and Planetary Science*
1048 *Letters*, 434, 298–307, <https://doi.org/10.1016/j.epsl.2015.11.049>, 2016.
- 1049 Petit-Maire, N. and Guo, Z. T.: Mid-Holocene climatic change and man in the present-day
1050 Sahara desert, in: *Quaternary Deserts and Climatic Change*, CRC Press, 1998.
- 1051 Pfeiffer, M., Spessa, A., and Kaplan, J. O.: A model for global biomass burning in preindustrial
1052 time: LPJ-LMfire (v1.0), *Geoscientific Model Development*, 6, 643–685,
1053 <https://doi.org/10.5194/gmd-6-643-2013>, 2013.

- 1054 Rachmayani, R., Prange, M., and Schulz, M.: North African vegetation–precipitation feedback in
1055 early and mid-Holocene climate simulations with CCSM3-DGVM, *Climate of the Past*, 11, 175–
1056 185, <https://doi.org/10.5194/cp-11-175-2015>, 2015.
- 1057 Reale, O. and Dirmeyer, P.: Modeling the effects of vegetation on Mediterranean climate during
1058 the Roman Classical Period: Part I: Climate history and model sensitivity, *Global and Planetary*
1059 *Change*, 25, 163–184, [https://doi.org/10.1016/S0921-8181\(00\)00002-3](https://doi.org/10.1016/S0921-8181(00)00002-3), 2000.
- 1060 Schmidt, G. A.: Oxygen-18 variations in a global ocean model, *Geophysical Research Letters*,
1061 25, 1201–1204, <https://doi.org/10.1029/98GL50866>, 1998.
- 1062 Schneider, R., Schmitt, J., Köhler, P., Joos, F., and Fischer, H.: A reconstruction of atmospheric
1063 carbon dioxide and its stable carbon isotopic composition from the penultimate glacial maximum
1064 to the last glacial inception, *Climate of the Past*, 9, 2507–2523, [https://doi.org/10.5194/cp-9-](https://doi.org/10.5194/cp-9-2507-2013)
1065 2507-2013, 2013.
- 1066 Sha, L., Ait Brahim, Y., Wassenburg, J. A., Yin, J., Peros, M., Cruz, F. W., Cai, Y., Li, H., Du,
1067 W., Zhang, H., Edwards, R. L., and Cheng, H.: How Far North Did the African Monsoon Fringe
1068 Expand During the African Humid Period? Insights From Southwest Moroccan Speleothems,
1069 *Geophysical Research Letters*, 46, 14093–14102, <https://doi.org/10.1029/2019GL084879>, 2019.
- 1070 Shanahan, T. M., McKay, N. P., Hughen, K. A., Overpeck, J. T., Otto-Bliesner, B., Heil, C. W.,
1071 King, J., Scholz, C. A., and Peck, J.: The time-transgressive termination of the African Humid
1072 Period, *Nature Geosci*, 8, 140–144, <https://doi.org/10.1038/ngeo2329>, 2015.
- 1073 Siegenthaler, U., Stocker, T. F., Monnin, E., Lüthi, D., Schwander, J., Stauffer, B., Raynaud, D.,
1074 Barnola, J.-M., Fischer, H., Masson-Delmotte, V., and Jouzel, J.: Stable Carbon Cycle–Climate
1075 Relationship During the Late Pleistocene, *Science*, 310, 1313–1317,
1076 <https://doi.org/10.1126/science.1120130>, 2005.
- 1077 Simard, M., Pinto, N., Fisher, J. B., and Baccini, A.: Mapping forest canopy height globally with
1078 spaceborne lidar, *Journal of Geophysical Research: Biogeosciences*, 116,
1079 <https://doi.org/10.1029/2011JG001708>, 2011.
- 1080 Singh, R., Tsigaridis, K., LeGrande, A. N., Ludlow, F., and Manning, J. G.: Investigating
1081 hydroclimatic impacts of the 168–158 BCE volcanic quartet and their relevance to the
1082 Nile River basin and Egyptian history, *Climate of the Past*, 19, 249–275,
1083 <https://doi.org/10.5194/cp-19-249-2023>, 2023.
- 1084 Singh, R., Koch, A., LeGrande, A. N., Tsigaridis, K., Ramos, R. D., Ludlow, F., Aleinov, I.,
1085 Ruedy, R., and Kaplan, J. O.: Modelling framework for asynchronous land-atmosphere coupling
1086 using NASA GISS ModelE and LPJ-LMfire: Design, Application and Evaluation for the 2.5ka
1087 period, <https://doi.org/10.5281/zenodo.13626434>, 2024.
- 1088 Sitch, S., Smith, B., Prentice, I. C., Arneth, A., Bondeau, A., Cramer, W., Kaplan, J. O., Levis,
1089 S., Lucht, W., Sykes, M. T., Thonicke, K., and Venevsky, S.: Evaluation of ecosystem dynamics,
1090 plant geography and terrestrial carbon cycling in the LPJ dynamic global vegetation model,
1091 *Global Change Biology*, 9, 161–185, <https://doi.org/10.1046/j.1365-2486.2003.00569.x>, 2003.

- 1092 Stocker, T. F., Qin, D., Plattner, G.-K., Tignor, M. M. B., Allen, S. K., Boschung, J., Nauels, A.,
1093 Xia, Y., Bex, V., Midgley, P. M., Alexander, L. V., Allen, S. K., Bindoff, N. L., Breon, F.-M.,
1094 Church, J. A., Cubasch, U., Emori, S., Forster, P., Friedlingstein, P., Gillett, N., Gregory, J. M.,
1095 Hartmann, D. L., Jansen, E., Kirtman, B., Knutti, R., Kumar Kanikicharla, K., Lemke, P.,
1096 Marotzke, J., Masson-Delmotte, V., Meehl, G. A., Mokhov, I. I., Piao, S., Plattner, G.-K., Dahe,
1097 Q., Ramaswamy, V., Randall, D., Rhein, M., Rojas, M., Sabine, C., Shindell, D., Stocker, T. F.,
1098 Talley, L. D., Vaughan, D. G., Xie, S.-P., Allen, M. R., Boucher, O., Chambers, D., Hesselbjerg
1099 Christensen, J., Ciais, P., Clark, P. U., Collins, M., Comiso, J. C., Vasconcellos de Menezes, V.,
1100 Feely, R. A., Fichefet, T., Fiore, A. M., Flato, G., Fuglestvedt, J., Hegerl, G., Hezel, P. J.,
1101 Johnson, G. C., Kaser, G., Kattsov, V., Kennedy, J., Klein Tank, A. M. G., Le Quere, C., Myhre,
1102 G., Osborn, T., Payne, A. J., Perlwitz, J., Power, S., Prather, M., Rintoul, S. R., Rogelj, J.,
1103 Rusticucci, M., Schulz, M., Sedlacek, J., Stott, P. A., Sutton, R., Thorne, P. W., and Wuebbles,
1104 D.: Climate Change 2013. The Physical Science Basis. Working Group I Contribution to the
1105 Fifth Assessment Report of the Intergovernmental Panel on Climate Change - Abstract for
1106 decision-makers; Changements climatiques 2013. Les elements scientifiques. Contribution du
1107 groupe de travail I au cinquieme rapport d'evaluation du groupe d'experts intergouvernemental
1108 sur l'evolution du CLIMAT - Resume a l'intention des decideurs, 2013.
- 1109 Strandberg, G., Brandefelt, J., Kjellstro" M, E., and Smith, B.: High-resolution regional
1110 simulation of last glacial maximum climate in Europe, *Tellus A: Dynamic Meteorology and*
1111 *Oceanography*, 63, 107–125, <https://doi.org/10.1111/j.1600-0870.2010.00485.x>, 2011.
- 1112 Strandberg, G., Kjellström, E., Poska, A., Wagner, S., Gaillard, M.-J., Trondman, A.-K., Mauri,
1113 A., Davis, B. a. S., Kaplan, J. O., Birks, H. J. B., Bjune, A. E., Fyfe, R., Giesecke, T., Kalnina,
1114 L., Kangur, M., van der Knaap, W. O., Kokfelt, U., Kuneš, P., Lata\ owa, M., Marquer, L.,
1115 Mazier, F., Nielsen, A. B., Smith, B., Seppä, H., and Sugita, S.: Regional climate model
1116 simulations for Europe at 6 and 0.2 k BP: sensitivity to changes in anthropogenic deforestation,
1117 *Climate of the Past*, 10, 661–680, <https://doi.org/10.5194/cp-10-661-2014>, 2014a.
- 1118 Strandberg, G., Kjellström, E., Poska, A., Wagner, S., Gaillard, M.-J., Trondman, A.-K., Mauri,
1119 A., Davis, B. a. S., Kaplan, J. O., Birks, H. J. B., Bjune, A. E., Fyfe, R., Giesecke, T., Kalnina,
1120 L., Kangur, M., van der Knaap, W. O., Kokfelt, U., Kuneš, P., Lata\ owa, M., Marquer, L.,
1121 Mazier, F., Nielsen, A. B., Smith, B., Seppä, H., and Sugita, S.: Regional climate model
1122 simulations for Europe at 6 and 0.2 k BP: sensitivity to changes in anthropogenic deforestation,
1123 *Climate of the Past*, 10, 661–680, <https://doi.org/10.5194/cp-10-661-2014>, 2014b.
- 1124 Swann, A. L., Fung, I. Y., Levis, S., Bonan, G. B., and Doney, S. C.: Changes in Arctic
1125 vegetation amplify high-latitude warming through the greenhouse effect, *Proceedings of the*
1126 *National Academy of Sciences*, 107, 1295–1300, <https://doi.org/10.1073/pnas.0913846107>,
1127 2010.
- 1128 Texier, D., De Noblet, N., Harrison, S. P., Haxeltine, A., Jolly, D., Joussaume, S., Laarif, F.,
1129 Prentice, I. C., and Tarasov, P.: Quantifying the role of biosphere-atmosphere feedbacks in
1130 climate change: Coupled model simulations for 6000 years BP and comparison with palaeodata
1131 for northern Eurasia and northern Africa, *Climate Dynamics*, 13, 865–882, 1997.

- 1132 Thomas, G. and Rowntree, P. R.: The Boreal Forests and Climate, *Quarterly Journal of the Royal*
1133 *Meteorological Society*, 118, 469–497, <https://doi.org/10.1002/qj.49711850505>, 1992.
- 1134 Thompson, A. J., Tabor, C. R., Poulsen, C. J., and Skinner, C. B.: Water isotopic constraints on
1135 the enhancement of the mid-Holocene West African monsoon, *Earth and Planetary Science*
1136 *Letters*, 554, 116677, <https://doi.org/10.1016/j.epsl.2020.116677>, 2021.
- 1137 Thonicke, K., Spessa, A., Prentice, I. C., Harrison, S. P., Dong, L., and Carmona-Moreno, C.:
1138 The influence of vegetation, fire spread and fire behaviour on biomass burning and trace gas
1139 emissions: results from a process-based model, *Biogeosciences*, 7, 1991–2011,
1140 <https://doi.org/10.5194/bg-7-1991-2010>, 2010.
- 1141 Tian, Y., Woodcock, C. E., Wang, Y., Privette, J. L., Shabanov, N. V., Zhou, L., Zhang, Y.,
1142 Buermann, W., Dong, J., Veikkanen, B., Häme, T., Andersson, K., Ozdogan, M., Knyazikhin,
1143 Y., and Myneni, R. B.: Multiscale analysis and validation of the MODIS LAI product: I.
1144 Uncertainty assessment, *Remote Sensing of Environment*, 83, 414–430,
1145 [https://doi.org/10.1016/S0034-4257\(02\)00047-0](https://doi.org/10.1016/S0034-4257(02)00047-0), 2002a.
- 1146 Tian, Y., Woodcock, C. E., Wang, Y., Privette, J. L., Shabanov, N. V., Zhou, L., Zhang, Y.,
1147 Buermann, W., Dong, J., Veikkanen, B., Häme, T., Andersson, K., Ozdogan, M., Knyazikhin,
1148 Y., and Myneni, R. B.: Multiscale analysis and validation of the MODIS LAI product: II.
1149 Sampling strategy, *Remote Sensing of Environment*, 83, 431–441,
1150 [https://doi.org/10.1016/S0034-4257\(02\)00058-5](https://doi.org/10.1016/S0034-4257(02)00058-5), 2002b.
- 1151 Tierney, J. E., Pausata, F. S. R., and deMenocal, P. B.: Rainfall regimes of the Green Sahara,
1152 *Science Advances*, 3, e1601503, <https://doi.org/10.1126/sciadv.1601503>, 2017.
- 1153 Tiwari, S., Ramos, R. D., Pausata, F. S. R., LeGrande, A. N., Griffiths, M. L., Beltrami, H.,
1154 Wainer, I., de Vernal, A., Litchmore, D. T., Chandan, D., Peltier, W. R., and Tabor, C. R.: On
1155 the Remote Impacts of Mid-Holocene Saharan Vegetation on South American Hydroclimate: A
1156 Modeling Intercomparison, *Geophysical Research Letters*, 50, e2022GL101974,
1157 <https://doi.org/10.1029/2022GL101974>, 2023.
- 1158 Velasquez, P., Kaplan, J. O., Messmer, M., Ludwig, P., and Raible, C. C.: The role of land cover
1159 in the climate of glacial Europe, *Climate of the Past*, 17, 1161–1180, [https://doi.org/10.5194/cp-](https://doi.org/10.5194/cp-17-1161-2021)
1160 [17-1161-2021](https://doi.org/10.5194/cp-17-1161-2021), 2021.
- 1161 Yang, W., Tan, B., Huang, D., Rautiainen, M., Shabanov, N. V., Wang, Y., Privette, J. L.,
1162 Huemmrich, K. F., Fensholt, R., Sandholt, I., Weiss, M., Ahl, D. E., Gower, S. T., Nemani, R.
1163 R., Knyazikhin, Y., and Myneni, R. B.: MODIS leaf area index products: from validation to
1164 algorithm improvement, *IEEE Transactions on Geoscience and Remote Sensing*, 44, 1885–1898,
1165 <https://doi.org/10.1109/TGRS.2006.871215>, 2006.
- 1166 Zeng, Z., Wang, D., Yang, L., Wu, J., Ziegler, A. D., Liu, M., Ciais, P., Searchinger, T. D.,
1167 Yang, Z.-L., Chen, D., Chen, A., Li, L. Z. X., Piao, S., Taylor, D., Cai, X., Pan, M., Peng, L.,
1168 Lin, P., Gower, D., Feng, Y., Zheng, C., Guan, K., Lian, X., Wang, T., Wang, L., Jeong, S.-J.,
1169 Wei, Z., Sheffield, J., Caylor, K., and Wood, E. F.: Deforestation-induced warming over tropical

1170 mountain regions regulated by elevation, Nat. Geosci., 14, 23–29,
1171 <https://doi.org/10.1038/s41561-020-00666-0>, 2021.

1172